Iron-Based Core-Shell Nanowires for Combinatorial Drug Delivery, Photothermal and Magnetic Therapy

Aldo Isaac Martínez-Banderas‡, 1, Antonio Aires‡,2, Marta Quintanilla2, Jorge A. Holguín-Lerma3, Claudia Lozano-Pedraza4, Francisco J. Teran4,5, Julián A. Moreno3, Jose Efrain Perez1, Boon S. Ooi3, Timothy Ravasi1, Jasmeen S. Merzaban1, Aitziber L. Cortajarena2,4,5, Jürgen Kosel3*.*

[1]Division of Biological and Environmental Sciences and Engineering, King Abdullah University of Science and Technology, Thuwal Jeddah, 23955-6900, Saudi Arabia.

[2]CIC biomaGUNE, Parque Tecnológico de San Sebastián, Paseo Miramón 182, 20014 Donostia-San Sebastián, Spain.

[3]Division of Computer, Electrical, and Mathematical Sciences and Engineering, King Abdullah University of Science and Technology, Thuwal Jeddah, 23955-6900, Saudi Arabia.

[4]iMdea Nanociencia, Campus Universitario de Cantoblanco, C\Faraday, 9, 28049 Madrid, Spain.

[5]Nanobiotechnology Unit (iMdea Nanociencia) associated with Centro Nacional de Biotecnología (CNB-CSIC), Campus Universitario de Cantoblanco, Madrid, 28049, Spain.

[6]Ikerbasque, Basque Foundation for Science, Mª Díaz de Haro 3, 48013 Bilbao, Spain.

KEYWORDS iron-iron oxide core-shell, nanowires, photothermal therapy, magnetic cancer therapy, drug delivery.

ABSTRACT

Combining different therapies into a single nanomaterial platform is a promising approach for achieving more efficient, less invasive and personalized treatments. Here, we report on the development of such a platform by utilizing nanowires with iron core and iron oxide shell as drug carriers and exploiting their optical and magnetic properties. The iron core

has a large magnetization, which provides the foundation for low-power magnetic manipulation and magneto-mechanical treatment. The iron oxide shell enables functionalization with doxorubicin through a pH-sensitive linker, providing selective intracellular drug delivery. Combined, the core-shell nanostructure features an enhanced light-matter interaction in the near-infrared region, resulting in a high photothermal conversion efficiency of >80% for effective photothermal treatment. Applied to cancer cells, the collective effect of the three modalities results in an extremely efficient treatment with nearly complete cell death (~90%). In combination with the possibility of guidance and detection, this platform provides powerful tools for the development of advanced treatments.

INTRODUCTION

The combination of therapeutic strategies into a single agent or platform is a promising approach towards more efficient, safer, and less invasive cancer treatments.[1-2] Nanotherapies triggered by stimuli based on remotely activated agents are attractive alternatives, compared to chemical or radiation therapies that are highly aggressive to the organism.[3] Selective subcellular delivery of pharmaceutical agents may increase the therapeutic efficiency and simultaneously overcome secondary effects. Nanomaterials have been employed to reach therapeutic dosing, establish sustained-release drug profiles,[4] and increase the half-life of drugs, avoiding efflux or degradation.[5]

Nanomaterials have shown interesting structural, optical and electromagnetic properties that together with their kinetic behavior can be modulated by their physical properties such as size, shape and surface functionalization.[4] Large amounts of therapeutic molecules, such as anticancer drugs, can be loaded onto their vast surface.[6] Thus, the potential of nanomaterials as therapeutic agents can be modulated and personalized by the biomedical properties of different surface coatings[7] and combined with the intrinsic electromagnetic or optical properties of the core material.[8] The biodistribution of colloidal suspensions of nanomaterials that are directly injected into the target area or the bloodstream could be potentially controlled with different targeting agents or remote manipulation via their electromagnetic properties.[9-10] In case of magnetic nanomaterials, a magnetic field can be used for their remote guidance,[11] rotation[12] or to induce heat.[13]

In the search for new treatments, the heat-sensitivity of cancer cells has been extensively exploited for tumor therapy[14] and recently with nanomaterials-mediated hyperthermia.[15] Heat losses of nanomaterials can be triggered remotely either by alternating magnetic fields[16] or by light irradiation.[17] In the latter case, this so-called photothermal therapy is based on the heat release from nanoparticles while irradiation with near-infrared (NIR) light, minimizing biological tissue damage.[18] Plasmonic nanomaterials made of gold,[19] silver[20] or copper[21] are the main candidates for photothermal therapy. Optical excitation causes local plasmonic heating that affects cancer cells in the direct vicinity of the nanomaterials, generating promising results both *in vitro*[18, 22] and *in vivo* in animal models.[18, 23-24] The efficiency of a nanomaterial to translate optical energy into heat is known as photothermal conversion efficiency.[25] This has been determined for different gold (Au) nanomaterials, which is the most widely used photothermal agent, reaching values from 60% to almost 100% for Au nanorods, Au/Au_2S

nanoshells, and Au nanostars. Thereby, a dependence on the geometry and dimensions of the nanomaterial was found.[26-28]

Iron (Fe) and iron oxide (Fe_xO_y) nanomaterials have been exploited for cell therapies since a long time, and their development for cancer treatment in the form of magnetic particle hyperthermia has reached the clinical trials.[29-31] These materials are highly biocompatible with a pronounced degradation and clearance *in vivo*; indeed, the body assimilates the ions released through a highly regulated process.[32-35] In addition, their magnetic properties allow the manipulation by magnetic forces[11, 15, 36] as well as tracking by magnetic resonance imaging.[37-40] This makes iron-based nanomaterials highly attractive for next-generation multifunctional platforms.

Several types of Fe_xO_y nanoparticles have been tested for photothermal therapy *in vitro* and *in vivo*. Their efficiency typically lags behind the one of their Au counterparts. For instance, 13 nm Fe/Fe_xO_y (core/shell) particles were reported with a conversion efficiency around 20% (808 nm, 0.3−0.4 W/cm^2),[40] 180 nm Fe_3O_4 chitosan-modified spherical particles induced a temperature change (ΔT) of about 54°C (808 nm, 2 W/cm^2),[41] highly crystallized 15 nm Fe_xO_y nanoparticles yielded a ΔT of 33°C (885nm, 2.5W/cm^2)[42], and nanoparticle clusters of 225 nm in diameter showed a ΔT of 51°C (808 nm, 5 W/cm^2).[43] Recently, Fe_3O_4 nanocubes were used for a dual treatment using magnetic and photothermal heating. The nanocubes were exposed to both, an alternating magnetic field (AMF) and NIR laser irradiation (808 nm, 0.3 and 0.8 W/cm^2) that highly amplified their heating effect.[44]

Magnetic Nanowires (NWs) are characterized by their large magnetic moments and saturation.[45] NWs composed of Fe have shown cellular internalization with high biocompatibility, even at high concentrations with long incubation periods.[46] Due to the NWs' shape anisotropy, forces and torques can be generated when a magnetic field is applied.[47-50] At low frequencies, a magneto-mechanical effect is produced by the oscillation of the NWs,[49] while a hyperthermia effect can be generated at high frequencies (~100 kHz)[51-52]. Magnetic NWs have been reported to induce cancer cell death through a magneto-mechanical effect by applying an AMF (0.4 kA/m, 1 Hz and 1 kHz, 10 min), where any temperature contribution was disregarded, since no temperature change was detected between the testing groups. Cell death was partially attributed to cell membrane rupture, due to the magneto-mechanical disruption exerted by the NWs.[47] Furthermore, the potential of doxorubicin (DOX)-functionalized Fe NWs for cancer treatment has been previously assessed *in vitro* by combining the chemotherapeutical effect of DOX, with the magneto-mechanical disturbance exerted by the NWs, when a low frequency AMF is applied (0.8 kA/m, 10 Hz, 10 min). An additive cytotoxic effect was found by the combinatory treatment, decreasing the cell viability by ~70%, an efficacy that was higher than the ones obtained by either strategy individually.[50]

Here, we report the first observation of the photothermal effect in NWs composed of an Fe core and an Fe_xO_y shell and study its efficacy for killing cancer cells. The optical properties of the core-shell NWs were characterized, and a photothermal efficiency that is competitive with Au-based structures was obtained. Their photothermal response inside breast cancer cells was evaluated by temperature measurements through a NIR thermal camera. Cell internalization and the effectiveness of the NWs as drug carriers were further corroborated. Finally, the combination of the chemotoxic, magneto-mechanical, and optical treatment modes with the functionalized core-shell NWs was evaluated through the decrease in cell viability of breast cancer cells, revealing an extremely high efficiency, exceeding the one of the individual treatments and the free chemotherapeutic treatment with the anticancer drug.

RESULTS AND DISCUSSION

Nanowire characterization

The physical and chemical properties of core-shell NWs composed of Fe used in this study have been previously described and reported.[50, 53] With a deposition time of 1.5 h, NWs with an average length of 6.4±1.3 μm (n=100) and a diameter of 30 to 40 nm were fabricated as observed in transmission electron microscopy (TEM) and scanning electron microscopy (SEM) images, respectively (Figure 1A). Since the NWs are exposed to air, water, sodium hydroxide, ethanol, etc., oxidation of their surface is unavoidable. The resulting Fe_xO_y layer is typically 4-7 nm thick,[46] composed of both Fe_3O_4 and Fe_2O_3,[50, 53] and has a significant contribution to the biocompatibility,[53] functionalizability,[46, 50, 54] and magnetic properties of the NWs.[55]

A sample of NWs was first coated with bovine serum albumin (BSA)[56]. Zeta potential changed to -58 mV upon coating, compared to +2.85 mV of bare NWs,[57] aiding the dispersion of the NWs by electrostatic interaction. The presence of the coating around the NWs has been previously confirmed[58] and improved the biocompatibility[50] and colloidal properties with a reduction of agglomeration and enhancement of the dispersion. A DOX derivative[50, 59] was bound to the BSA coated NWs (NWs_DOX) through a pH-sensitive, covalent bond that allows the selective release of the unmodified drug, when exposed to intracellular conditions (pH = 5 in endosomes/lysosomes).[6, 60] The release kinetics of DOX from the functionalized NWs (identical to the ones used in this study) has been previously reported.[50] A DOX release of 80% was observed, when placing the NWs in an acidic environment after 2 h, in comparison to the minor release observed, when the NWs remained in a solution at neutral pH. Due to several sonication processes that break the NWs apart during the functionalization process, the length of the NWs was reduced to 3.0 ± 1.2 μm (Figure 1B).

The magnetization curve of the NWs inside the alumina membrane is shown in Figure 1C. The values of the saturation magnetization and the coercive field are 164 Am^2/kg and 105 kA/m, respectively, for a field applied parallel to the NWs. Similar values for the saturation magnetization (M_S) have been reported for Fe NWs before,[46] and they are lower than the one of bulk Fe at room temperature (218 Am^2/kg).[61] The difference is caused by the presence of the oxide layer surrounding the NWs. Magnetization measurements of core-shell NWs composed by Fe with different oxidation levels revealed that the saturation and remanent magnetizations depend on the oxide interphase thickness.[53] It is important to note that the magnetization loop of a single NW deviates considerably from the one of an array, because of the magnetostatic interaction between the NWs inside of the template. Single Fe NWs demonstrated single domain properties, and therefore are permanently magnetized with the magnetic remanence value being equal to the one of M_S measured in the parallel direction.[45]

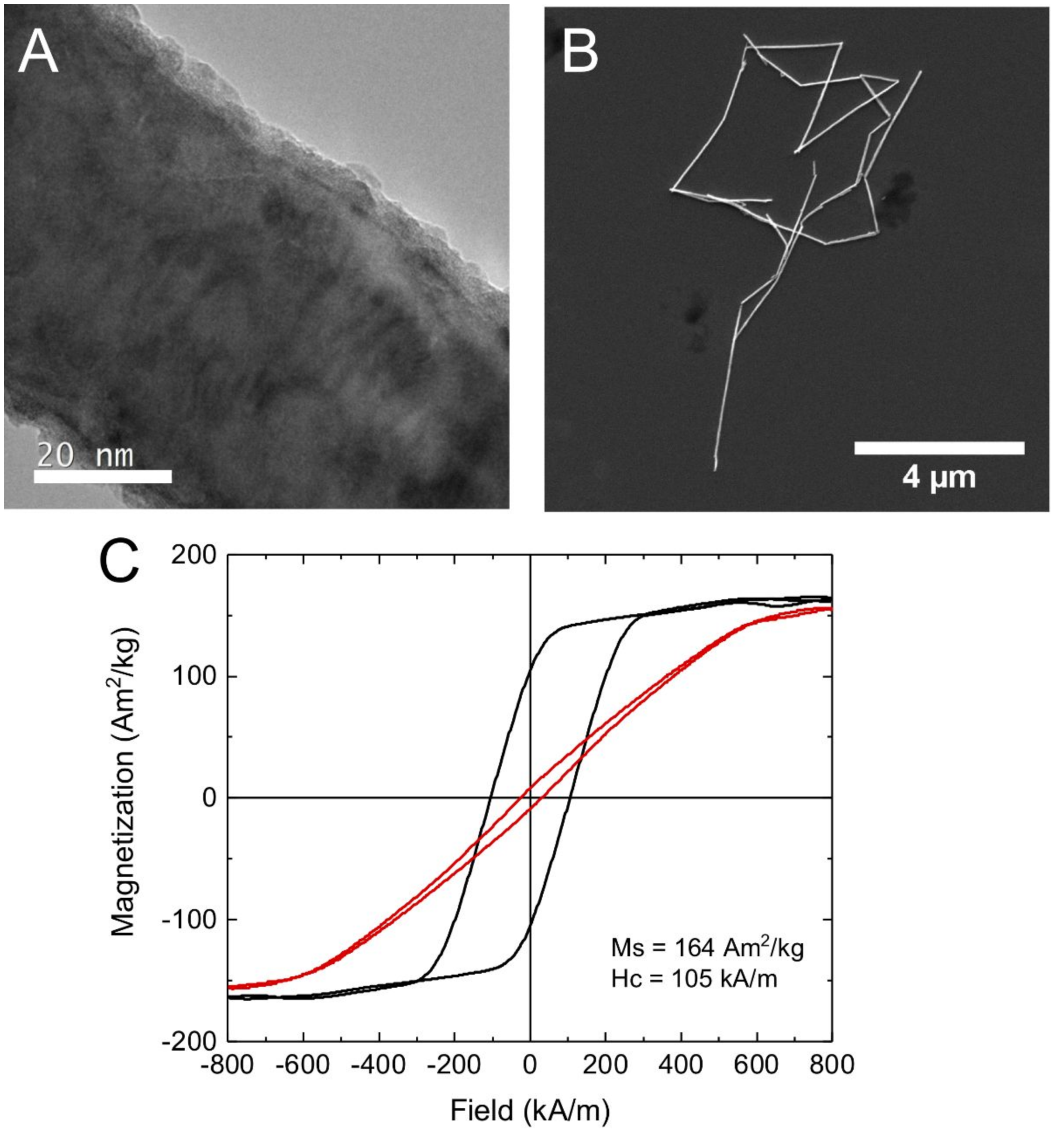

Figure 1. Characterization of Fe-Fe_xO_y core-shell NWs. (A) TEM image of a single NW. (B) SEM image of NWs on a silicon substrate after functionalization. (C) Magnetization curves of NWs embedded in the alumina membrane with the NWs placed parallel (black curve) and perpendicular (red curve) to the direction of the applied magnetic field (M_S is the saturation magnetization and H_C the coercive field, n = 3).

A sample of core-shell NWs was subjected to oxidizing conditions and its chemical composition compared with the one of NWs with a native oxide layer. The electron energy loss spectroscopy (EELS) composition maps in Figure S1 confirms a core-shell structure with an Fe core (Figure S1AII and S1BII) surrounded by an Fe_xO_y shell (Figure S1AIII and S1BIII). Moreover, the EELS map of the sample subjected to oxidizing conditions shows an increase in the thickness of the Fe_xO_y shell with ~10 nm (Figure S1BI to S1BIV) in comparison to the NWs with native Fe_xO_y layer with a thickness of ~5 nm (Figure S1AI to S1AIV). This shell can be identified in the Fe map (Figure S1BII), where a layer of lower color intensity is observed at the edges of the NW, which exactly overlaps with the oxygen map (Figure S1BIII). The oxide shell displays a constant thickness, in contrast to the sample with a native oxide layer that appears more diffuse. Furthermore, Figures S1BIII and S1BIV indicate an apparent increase of oxygen in the core region. Full oxidation of NWs composed of Fe, such as the ones employed in this study, has been previously corroborated using similar oxidizing conditions.[53]

Photothermal efficiency

The absorption spectra of aqueous solutions of both core-shell NWs, with thick and native Fe_xO_y shell (Figure 2A) show that the absorption (i.e. the optical density) gradually decreases from the ultraviolet through the visible region (300 nm to 700 nm) down to to the NIR region (>700 nm) for both NW samples. This trend is in agreement with reported spectra of different Fe-based and Fe_xO_y-based nanomaterials.[40-41, 62-63] Even though the light absorbance of both core-shell NWs is lower for the NIR compared to the visible range, deep light penetration into the biological tissue occurs only in the NIR range,[64] hence, this range is the most interesting one.

The inset of Figure 2A shows that at the 808 nm wavelength region the NWs with native oxide shell (Figure 2A, blue line) exhibit an absorption ~27% higher than that of the oxidized NWs (Figure 2A, black line). From the absorption spectra, the extinction coefficients (at 808 nm) for NWs with native Fe_xO_y shell and oxidized NWs were calculated to be ~922 L/mol·cm and ~680 L/mol·cm, respectively. The absorbance spectra of previously reported nanoparticles composed of Fe measured at different time points during oxidation process display the same trend. Sligthly oxidized nanoparticles, analogous to our NWs with their Fe-Fe_xO_y core-shell structure, showed higher absorption in the NIR range compared to the same nanoparticles at a longer oxidation time.[65] Altogether, these results confirm that the presence of both Fe and Fe_xO_y have an influence on the optical properties of nanomaterials.

The optical absorption spectra of different Fe_xO_y nanocrystals have been explained by the charge transfer and ligand transitions of Fe in its oxidized forms[63]. However, the role of the solid Fe core on the optical properties of core-shell Fe-Fe_xO_y nanoparticles has not been described in the past.

In general, the fate of light incident onto the surface of Fe dependes on its wavelength. High-energy light will be absorbed at specific energy transitions of Fe such as the first ionization energy (~7.9 eV)[66] or the workfunction (~4.5 eV).[67] Since the energy of the light at 808 nm (1.53 eV) is lower than the work function or the ionization energies of Fe, most of the light will be reflected or scattered, due to the electric field component.[68] However, given the physical confinement at the nano-scale (e.g. the short-axis of the NWs) the electrons in the Fe core are still subject to oscillations and dipoles created by the alternating electric field of the incident light. This leads to significant electron-electron and electron-phonon interactions similar to the ones described for noble metals.[69] These types of interactions are weaker in semiconductors such as Fe_xO_y, due to the lower amount of free electrons and phonons participating in the conduction phenomena. A clear example of this difference is illustrated by the thermal conductivity, depicting values of 80 W/m·K for Fe,[70] and <7 W/m·K for Fe_xO_y.[71] Other nanoscale-related effects such as photon trapping and photon localization[72] as well as interfacial effects such as metal-oxide band alignment and electron transport[73] can lead to increased light-matter interactions in core-shell structures in contrast to pure Fe_xO_y nanoparticles.

As compared to Au-based nanoparticles coated with Fe_xO_y, the energy needed to move electrons from the metal to the oxide is lower in the case of Fe-Fe_xO_y core-shell nanoparticles. The work function of Au (Φ_{Au} ~ 5.1 eV) is larger than the one of Fe (Φ_{Fe} ~ 4.5 eV),[67] giving rise to a lower potential barrier for the electrons in the Fe core to difusse into the conduction band of the oxide shell upon light excitation. This is normally correlated to an enhanced photocatalytic activity[74] and will lead to recombinations related to the photothermal effect.[75] An electromagnetic wave traveling into an Fe-Fe_xO_y core-shell NW will first interact with the oxide shell, where it gets partially absorbed, then it will interact with the metal, partly being subject to reflection, and then it will interact again with the oxide in a multi-absorption path. Meanwhile, in the case of pure Fe_xO_y nanoparticles, light travels in a single-pass absorption event, whereas pure Fe nanoparticles could reflect most of the light. In order to evaluate this theory, finite element method simulations were performed by comparing core-shell Fe NWs with different thickness of the oxide shell and evaluating the amplitude of the electric field originating from the electromagnetic wave interacting with the sample (Figure 2B). For simplicity we used the cross-section of the NWs to illustrate the short-axis (i.e. the in-plane vectors), while the out-of-plane vector corresponds to the long-axis of the NWs. As seen in Figure 2B, a laser light with a wavelength of 808 nm is projected along the y-axis in order to interact with three different types of NWs. The images in the top row show the detail of the interaction, whereas the images in the bottom row show the projection path of the light and the intensity profile at a distance of 0.5 μm after the NWs. In Figure 2BI, a NW made of only Fe_xO_y concentrates the electric field of the incident light (E = 1 V/m) up to 1.9 times, due to the dipole created under the influence of the alternating electric field from the light. There is very low reflection (i.e. subtle interference patterns) and most of the incident light is undisturbed.

The later effect can be observed from the intensity profile after interaction with the NW, showing a Gaussian distribution closely similar to the one exhibited by the same laser light in an obstacle-free path (i.e. without NW interaction), shown as a dotted line in the plot. In Figure 2BII and Figure 2BIII, Fe-Fe_xO_y core-shell NWs with a thick oxide shell (10 nm) and with a thin oxide shell (5 nm) showed an increase in the strength of the electric field by a factor of ~3.9 and ~3, respectively. These values represent an increase of 51% and 37% as compared to the NW composed of only Fe_xO_y. This enhancement of the light-matter interaction among the core and the shell has been observed on metal-semiconductor NW structures designed to improve the light absorption of semiconductors.[76] In a similar way, as seen in the simulations, the peak intensities of the electric field are found within the oxide shell giving rise to a potential enhancement of the photothermal effect. A model of a NW made of pure Fe (i.e. without any oxide shell) reveals a concentration of the electric field of up to ~8.8 times of the incident beam (Figure S2). This is expected from the strong interaction of electromagnetic waves with the electron density of the metal. Even though this could be attractive as a potential photothermal agents, an oxide layer is unavoidable in reality. Moreover, the strong interaction of light with the elemental Fe can be responsible for reducing the penetration of light through an array of NWs, limiting the depth and the number of NWs involved in the light-matter interaction. These findings highlight the novelty of utilizing Fe-Fe_xO_y core-shell NWs.

Figure 2BII and Figure 2BIII also reveal interference patterns, due to the significant reflection from the Fe core, as well as scattering that can be seen in the perturbed intensity profile of the light after interaction with the core-shell NWs. These phenomena is expected to enhance the overall absorption in randomly dispersed NWs by achieving multiple absorption events, where the light that is being reflected from one NW would be recycled towards another NW. Additional considerations such as a the high refractive index contrast (Fe_3O_4: $n \sim 2.3$; Fe_2O_3: $n \sim 2.8$; compared to blood and tissue: $n \sim 1.3$)[77-79] and the energy band alignment at the Fe-Fe_xO_y interface, could potentially benefit the light guiding, photon trapping, electron diffusion, and electron-phonon interaction, leading to an increased phototermal effect in the oxide shell. A summary of the proposed light-NW interaction is shown in Figure 2C.

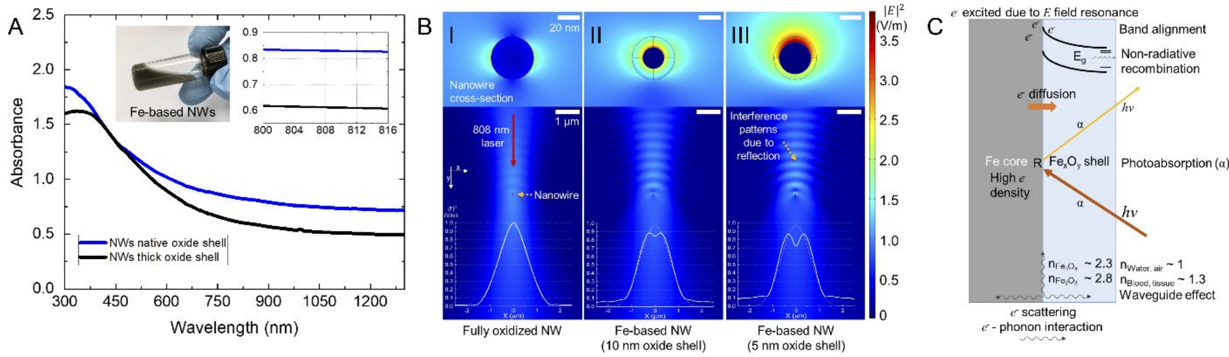

Figure 2. Optical characterization of Fe-Fe_xO_y core-shell NWs with different oxidation level. (A) Optical absorption spectra of aqueous solutions of Fe-Fe_xO_y core-shell NWs with native oxide layer (blue) and exposed to oxidizing conditions (black), both at the Fe concentration of 0.05 mg of Fe/mL. Insets show an aqueous solution of Fe NWs (left) and a magnification of the region of interest (right). (B) Simulation of the light absorption in NWs with different oxidation levels showing the intensity of electric field generated by the interaction of a focused laser light (808 nm) and the cross-section of the NWs. The top row shows the vicinity of the NWs and the bottom row shows the light path and intensity profile of the incident light after interaction with (BI) a fully oxidized NW, (BII) a model of the NW exposed to oxidizing conditions (Fe_xO_y shell = 10 nm), and (BIII) a model of the NW with native oxide shell (Fe_xO_y shell = 5 nm). For comparison, the electric field profile of the laser light without obstacles (i.e. without NWs) is plotted as dotted line. (C)

Proposed phenomena of the light-matter interaction for Fe-Fe_xO_y core-shell NWs upon light exposure, leading to increased light absorption and augmented photothermal effect.

The core-shell NWs with native oxide layer (~5 nm thick) were chosen for further experiments, due to the higher absorption observed at 808 nm in comparison with NWs exposed to oxidizing conditions. Infrared thermography images from the NW suspensions are shown in Figure 3A. A significant difference in the temperature is observed between the image of the phosphate buffer saline (PBS) solution (0 mg Fe/mL, Figure 3AI) and the NW suspensions in PBS containing 0.02, 0.04, and 0.20 mg Fe/mL in quartz micro-cuvettes during the laser irradiation (Figure 3AII-3AIV) that increased with the Fe concentration. The average temperatures of the solutions were calculated from the area within the cuvette, indicated by yellow squares (9 mm x 2 mm) in each sample, and were plotted as a function of time (Figure 3B). After 2 min, a ΔT of about 13°C was measured in the solution with the highest NW concentration (0.2 mg Fe/mL), whereas the solution with 10 times less NW content showed a ΔT of approximately 4°C. These results confirmed that the heating occurred by the NWs present in the solution, as the control sample, containing only PBS, showed a ΔT of only 2°C. Cyclic measurements of the initial and final temperature of a NW solution in PBS (0.2 mg Fe/mL) throughout 5 consecutive days show no decrease in the photothermal response of the NWs, indicating stability after multiple irradiation sessions (Figure S3).

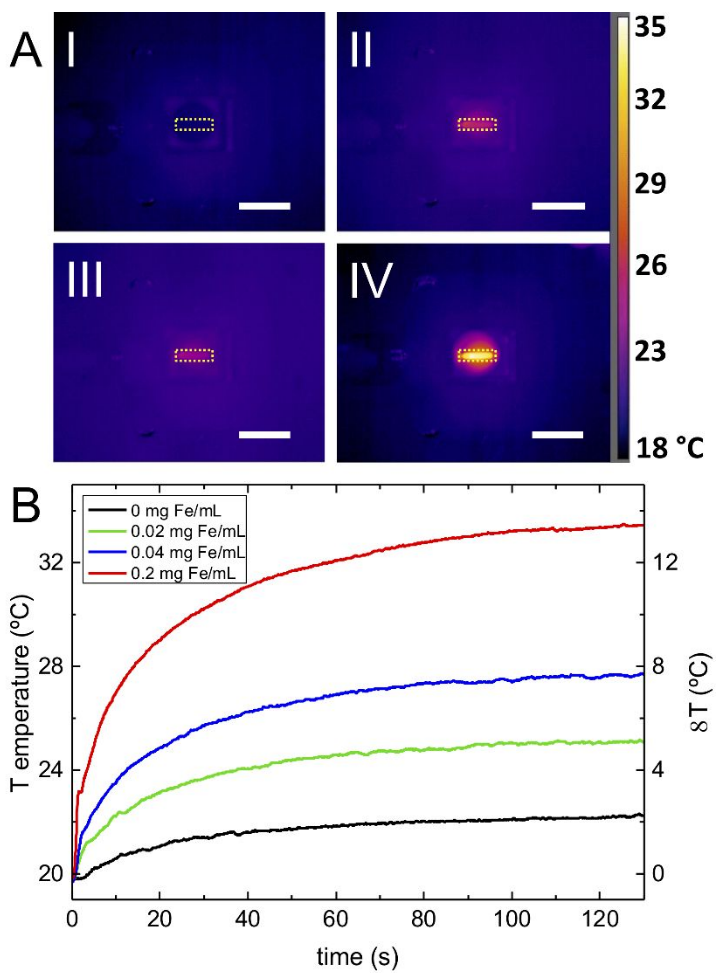

Figure 3. Photothermal effect of Fe-Fe_xO_y core-shell NWs. (A) Thermal images of the NW solutions in quartz micro-cuvettes acquired with an IR camera. (AI) PBS solution before laser irradiation. (AII) to (AIV) samples with 0, 0.02 and 0.20 mg Fe/mL, respectively, after 2 min of NIR laser irradiation at 808 nm. The laser was applied with 0.8 W/cm^2, and the images show top views of the samples. The yellow rectangles indicate the area from which the average temperature was calculated. Scale bar = 1 cm. (B) Temperature response of the NW suspensions, when irradiated with a NIR laser (808 nm) at the concentrations of 0, 0.02, 0.04, and 0.20 mg Fe/mL.

The efficiency of core-shell NWs to convert optical energy into heat was determined by calculating the photothermal conversion efficiency as explained in the Methods section. From the temporal response curves of each NW solution, when cooling down, the characteristic thermal time constant of the system was determined (Figure S4). This thermal time constant was correlated to a linearized heat transfer coefficient (Equation 5) that can, in turn, be used to calculate the amount of heat energy accumulated in or lost from the sample, given the temperature inside (Equation 3 and 4). The calculated parameters are summarized in Table S1. An average efficiency value of 83% was found for the three NW solutions. This value is in the same range as those obtained for Au-based nanoparticles, Au nanorods, Au/Au_2S nanoshells, and Au nanostars at similar irradiation conditions.[26-28] The photothermal conversion efficiency of the solution decreases with increasing NW concentration, which can be explained by a reduction in the light penetration when increasing the NW concentration, as the laser beam is attenuated by the NW suspension.

Additionally, the specific loss power (SLP) was determined, considering the dynamical temperature curves of each NW suspension shown in Figure 2C, from which the slope at initial times after NIR irradiation (Figure S5) was used together with the specific heat capacity and mass of the suspension components (Equation 6, see Supporting Information). The calculated SLP values range from 121.7±1.3 kW/g Fe to 74.4±0.7 kW/g Fe for NW dispersions with Fe contents of 0.02 and 0.2 mg Fe/ml, respectively (Table S2). The reason for the decrease in the SLP value at higher concentrations is again attributed to the increased laser beam attenuation by the NW suspension. Although the temperature response curves in Figure 2C were obtained in non-adiabatic conditions, which significantly influence the temperature slope at initial times during NIR irradiation,[80-83] the SLP values of core-shell Fe-Fe_xO_y NWs remained much higher than those reported for other Fe_xO_y nanoparticles.[44, 84-88]

Cellular internalization

Studies on the cellular uptake and degradation of NWs similar to the ones employed in this study have been previously reported.[89-90] In this study, NWs internalization on breast cancer cells was assessed through inductively coupled plasma mass spectrometry (ICP-MS) measurements and confocal reflection microscopy. From the ICP measurements, an average Fe mass of 42±2 and 115±2 pg Fe/cell was quantified for cells incubated with 0.01 or 0.02 mg of Fe/mL of core-shell NWs coated with BSA. This internalization represents ~60% and ~79% of the NW mass dispersed in the cell media for incubation, respectively. It should be noted that these values refer not only to internalized NWs but also to NWs embedded in or adsorbed on the extracellular structures surrounding the plasma membrane.

Confocal reflection microscopy images of internalized BSA coated NWs in breast cancer cells were taken after 24 h of incubation with 0.01 mg Fe/mL (Figure 4AI to 4AIII) or 0.02 mg Fe/mL (Figure 4BI to 4BIII) with n = 3 in both cases. This method exploits the ability of the NWs to reflect light at a wavelength of 488 nm and has been successfully implemented before to study the internalization of NWs in MDA-MB-231 cells.[50] The BSA coated NWs, which are shown in green, were colored with ZEN-ZEISS imaging software, and the nucleus, shown in red, was stained with NucRed™ Live 647 (ThermoFisher). A considerably larger number of NWs appeared in the cells incubated with 0.02 mg Fe/mL. Previous studies utilizing NWs with similar dimensions show that cellular internalization is a continuous process that starts upon contact between NWs and cells,[57] and takes place through the activation of the integrin-mediated phagocytosis pathway.[48, 91] Frustrated phagocytosis, that could led to inflammatory process *in vivo*, has been observed in cells incubated with longer NWs (>14 μm).[92] Perez et al., 2016 have reported that internalized NWs were observed inside endosomes 24 h post incubation and that a minimal fraction (~2%) of them dissolved intracellularly after 72 h due to the acidic environment of the lysosomal compartments in the cytoplasm.[49]

In order to investigate the subcellular location of the DOX functionalized NWs after endocytosis, confocal microscopy was performed after 48 h of incubation (Figure S6, Supporting videos S1 and S2). The NWs were monitored by confocal reflection mode, the nucleus and endosomes/lysosomes were stained with NucRed™ Live 647 (ThermoFisher), and the released DOX was monitored by its fluorescence (Figure S6). Confocal fluorescence imaging corroborated the cellular internalization of the NWs, which mostly co-localized with the endosomes/lysosomes. It also confirmed that DOX was internalized with the NWs and was released after 48 h post incubation, when it started to accumulate inside the endosomes/lysosomes.

Furthermore, localization of DOX in the nucleus was observed after 72 h of incubation of the cells with the functionalized NWs (Figure S7).

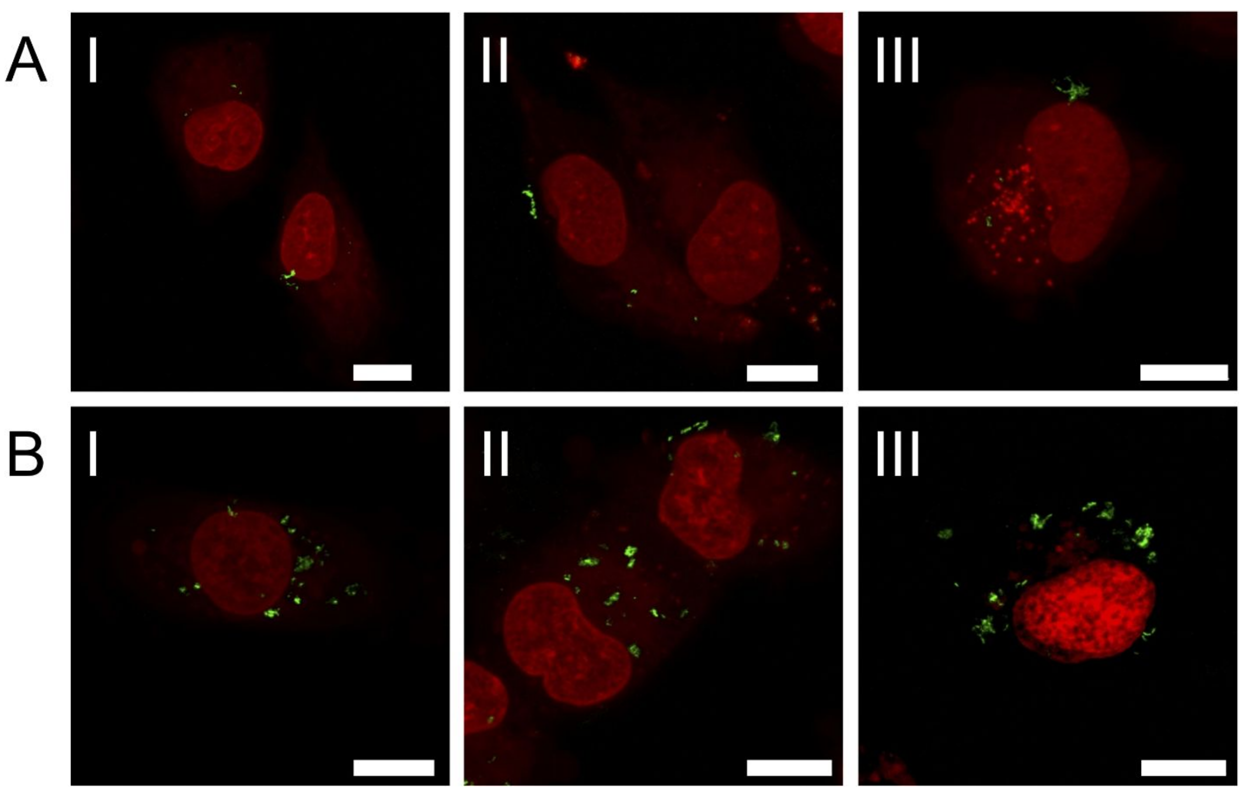

Figure 4. Confocal microscopy images of MDA-MB-231 cells incubated with BSA coated NWs. Cell incubated with BSA coated NWs after 24 h with a concentration of 0.01 mg Fe/mL (AI-AIII) and 0.02 mg Fe/mL (BI-BIII). Scale bars = 10 µm. NWs through light-reflected signal are shown in green and were pseudo-colored using ZEN-ZEISS imaging software. The nucleus, shown in red, was stained with NucRed™ Live 647. These are representative images of 3 independent experiments for each NW concentration.

Photothermal effect of nanowires in cancer cells

The photothermal conversion effect of the BSA coated NWs inside cells was evaluated by using a concentrated suspension of breast cancer cells (1.5×10^6 cells/mL) after being incubated with the NWs at a concentration of 0.02 mg Fe/mL. A concentrated cell suspension with no internalized NWs was used as a negative control. The concentrated cellular suspensions inside a well of a 96 well plate were irradiated with an 808 nm laser at 0.8 W/cm^2 for 10 min at room temperature, and the temperature was monitored with an IR thermal camera fixed above the samples (Figure 5). As shown in Figure 5A, thermal images from both the control and the NW-incubated cell suspensions before and during the laser irradiation were acquired, and the temperature profiles were plotted in Figure 5B. During irradiation, the NW-incubated cell suspension reached a temperature of almost 40°C (Figure 5AIV), which is translated into a ∆T of ~20°C, whereas control cells (Figure 5AII) showed only a slight temperature increase of ~2°C. This result indicates that intracellular confinement did not hinder the photothermal conversion of NWs when a high cell density is used.

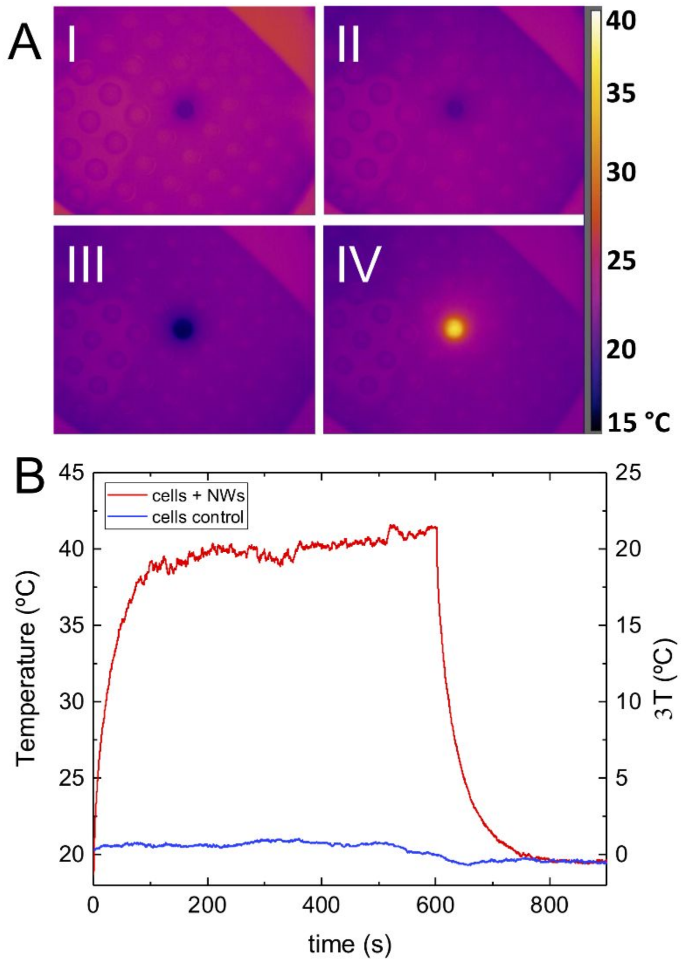

Figure 5. Photothermal effect of BSA coated NWs in breast cancer cells. (A) Thermal images acquired with an infrared camera of a concentrated suspension of breast cancer cells. Cells without NWs before (AI) and after (AII) NIR laser irradiation. Cells incubated with BSA coated NWs before (AIII), and after (AIV) NIR laser irradiation. The laser was applied with a power density of 0.8 W/cm2, and the images correspond to the view from the top of a 96 well plate. (B) Temperature response curves of concentrated suspensions

of breast cancer cells non-incubated (control) and incubated with BSA coated NWs (0.02 mg Fe/mL) that were irradiated with a NIR laser (808 nm).

A notable difference is observed between the temperature change with the dense cellular suspension (initially incubated with NWs at a concentration of 0.02 mg Fe/mL; Figure 5B; ΔT = 20°C) and the aqueous suspension of NWs (Figure 3B; ΔT = 5°C; 0.02 mg Fe/mL), which can be explained by the smaller volume in which the cells remained after being concentrated into a pellet that is equivalent to increase the NWs concentration. The temperature change of the dense suspension of cells with internalized NWs was even higher than the one observed in the NW solution with a concentration that is 10 times higher (0.2 mg Fe/mL, ΔT = 13°C). Considering the dynamical temperature curves from Figure 5, the temperature slope at initial times after NIR irradiation was obtained (Figure S8), and together with the specific heat capacity and mass of the cell suspension components (Equation 7, see Supporting information), the SLP of the NWs inside breast cancer cells was estimated with a value of 5.0 ± 0.1 kW/g Fe. In addition, from the NW mass inside cells (i.e., 115±2 pg Fe/cell), the average heat released by the NWs per cell under irradiation at the mentioned exposure conditions can be determined. This average heat dose per cell (HDC)[93] is the product of SLP, Fe mass per cell, and heat exposure time (i.e., irradiation time) resulting in HDC = SLP$\cdot m_{FeCell}\cdot t_{irrad}$ = 345 ± 30 μJ per cell (see Supporting Information for parameter values). As mentioned above, the non-adiabatic conditions and strong conduction losses during the measurement of the temporal response curves affect the estimated SLP of NWs inside breast cancer cells and therefore the HDC.[81-82] Recently, a 40% decrease of the temperature slope at initial times has been shown, when the temporal response curves were recorded in the absence of vacuum shield (i.e. high conduction thermal losses of the sample holder).[83] Hence, the calculated HDC value is smaller than the real one, due to the experimental limitations of the calorimetric set-up for accurately determining the SLP value of the BSA coated NWs inside cells under non-adiabatic conditions.

Combinatorial treatment

The ability of the functionalized core-shell NWs to induce cancer cell death by combining the selective drug release with both, the mechanical disturbance exerted by the NWs upon the application of an AMF (8 kA/m, 10 Hz for 10 min) and the irradiation with an NIR laser (808 nm, 0.8 W/cm^2 for 10 min) was examined on MDA-MB-231 breast cancer cells using Alamar Blue assays with n = 4 in each experimental condition (Figure 6). Cultured cells in the absence of NWs and empty wells were used as positive and negative controls, respectively. Neither of the applied treatments, i.e., AMF, NIR laser irradiation or a combination of the two reduced the cell viability of cultured breast cancer cells in the absence of NWs. Cancer cells were also incubated with free DOX at a concentration of 1 μM, which reduced the cell viability by ~75%. The chemotoxic effect of the free anticancer drug was not affected by the application of the AMF and/or the NIR laser irradiation.

BSA coated NWs did not show any cytotoxic effect, when no external stimuli were applied at the time periods used in this study, confirming their excellent biocompatibility. A decrease of ~28%, 22%, and 34% in cell viability was observed for cells treated with BSA coated NWs (0.02 mg Fe/mL), when the NIR laser irradiation, AMF, and combinatory treatment were applied, respectively. The combination of the NIR laser irradiation and AMF has a slightly stronger effect on reducing cell viability than the independent treatments and there is a similar efficiency between NIR laser irradiation and AMF induced stress, which we attribute to the fact that only a certain number of cells internalize enough NWs to be sensitive to the photothermal effect and/or the magneto-mechanical disruption. It is important to note that no temperature change is expected by applying the AMF at the frequency and field strength employed.[47, 49, 51-52] This was confirmed by a control test, where the temperature of a NWs solution (0.2 mg Fe/mL) remained constant, when the AMF (8 kA/m, 10 Hz for 10 min) was applied for 10 min.

In the case of DOX_NWs (0.02 mg of Fe/mL with 1 μM DOX), the cytotoxic effect, due to the DOX release, showed a decrease of approximately 40% in cell viability. It is noticeable that the cytotoxic effect of the free DOX is higher than the one triggered by the released drug from the NWs. However, the important feature is that the NWs act as nano drug-delivery vehicle, and DOX can only be released when the NWs are located in endosomes after the internalization, ensuring a selective release,[6, 60] as observed in Figure S6 and Figure S7. This, in turn, prevents the appearance of side effects arising from the non-specific effect of DOX in an *in vivo* scenario,[56, 94] and the development of drug resistance.[95]

Combining the chemotoxic action with the laser irradiation and the AMF resulted in a decrease of ~76% and ~54%, respectively. The combination of the anticancer drug with the NIR laser irradiation is significantly more effective than the combination of DOX and AMF. We assume that the temperature increase from the photothermal treatment enhances the cytotoxicity probably by increasing the susceptibility of the cancer cells to the effect of DOX. Through our experimental design, we cannot assess if the laser irradiation induces the release of the DOX. However, the cell viability was measured 72 h after the adding the NWs, ensuring the release, localization of DOX in the nucleus[50] and maximum chemotoxic effect. Thus, any contribution to the rate of drug release through the photothermal or magneto-mechanical treatments can be disregarded.

Finally, the combination of the three treatments, i.e., DOX, NIR laser irradiation, and AMF, yielded a highly efficient additive cytotoxic effect. A reduction in the cell viability of ~91% was observed when applying the combinatory treatment to the cells incubated with NW_DOX that increased the cytotoxic effect by 15% and 30% when compared to the bimodal treatments of DOX in combination with NIR laser irradiation and AMF, respectively. This treatment is even more efficient than the free anticancer drug at the same concentration.

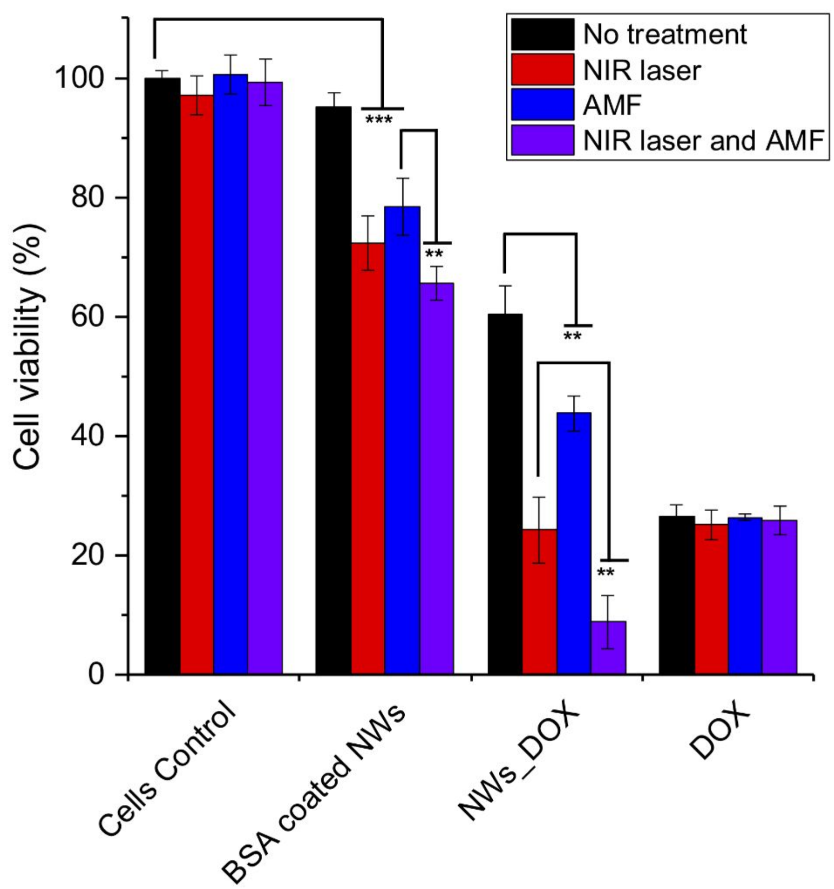

Figure 6. Viability of MDA-MB-231 cells incubated with different formulations of Fe-Fe_xO_y core-shell NWs with or without application of a low power AMF and/or NIR laser irradiation. BSA coated NWs: 0.02 mg Fe/mL, NWs_DOX: 0.02 mg Fe/mL and 1 μM of DOX. Free DOX: 1 μM. (*p < 0.05, **p < 0.01, and ***p < 0.001; n = 4).

CONCLUSION

Fe-Fe_xO_y core-shell NWs are nanomaterials with attractive properties for biomedical applications, due to their ability to interact with cells in various ways. This provides different control mechanisms, which can be remotely applied by magnetic fields or, as shown in this work, laser light. NWs combine low cytotoxicity with large surface areas, magnetization values, and photothermal efficiency. While their magnetic properties have been explored for killing cancer cells before, their optical properties have not been employed yet. In this work, the potential of core-shell NWs for photothermal treatment has been evaluated using NIR laser-mediated heating. We found an extremely high photothermal conversion efficiency of more than 80%, which is in the range of the best Au-based nanomaterials. This photothermal conversion efficiency was translated into a large intracellular heat dose. The efficiency of the NWs' photothermal effect was further supported by the outstanding SLP values of NWs in aqueous solution and inside breast cancer cells. The Fe-Fe_xO_y core-shell structure of our NWs was found to be essential for their photothermal efficiency through the enhancement of the light-matter interaction, when compared to pure Fe_xO_y NWs. Finally, the multifunctional capability of the NWs was explored for cancer cell destruction by combining the chemotherapeutic effect of DOX-functionalized core-shell NWs with their optical and magnetic properties. The combinatory treatment resulted in nearly complete cancer cell death and was more effective than individual or bimodal strategies. In case of the latter, either the magneto-mechanical effect or the photothermal therapy with the chemotoxic effect of DOX delivered to cancer cells by the NWs were combined. The combination of the chemotoxic, magneto-mechanical and optical treatment modes was found to have synergistic effects and led to a higher cytotoxic effect than the free DOX at the same concentration. The treatments employed require low power magnetic fields and low laser power density, avoiding the need for large and complex equipment and favoring further translation into clinical application. Utilizing the different control mechanisms of the core-shell NWs individually or in combination provides new avenues for personalized medical treatments. With the additional possibility of tracking by magnetic resonance imaging, the core-shell NWs have immense potential for developing advanced nanotherapies and theranostic applications.

METHODS

The main aspects of the methods are mentioned in this section. For detailed explanations of some of the procedures see the Supplementary Information.

Chemical reagents: Bovine serum albumin (BSA) and doxorubicin (DOX) were purchased from Sigma-Aldrich. Double distilled water was used in all experiments. A DOX derivative [(5-Maleimidovaleroyl) hydrazone of Doxorubicin] was synthesized as previously described[94] using as precursor 5-aminovaleric acid instead of 6-aminocaproic acid, to functionalize the coated NWs with DOX. ^{1}H NMR (400 MHz, MeOD, δ): 7.92 (bd, IH), 7.81 (t, IH), 7.55 (d, IH), 6.57 (m, 2H), 5.51 (m, IH), 5.07 (m, IH), 4.54 (d, IH), 4.25 (m, IH), 4.06 (s, 3H), 3.61-2.7 (m, 5H), 2.55-2.26 (m, 4H), 2.20-1.90 (m, 3H), 1.62-1.25 (m, 10 H); HRMS (ESI) m/z: $[M+H]^+$ calculated for $C_{36}H_{41}N_4O_{13}$, 737.2664; found, 737.2638.

Cell culture: The MDA-MB231 cell line was purchased from American Type Culture Collections (Manassas, VA, USA). Cells were grown as a monolayer in Dulbecco's Modified Eagle's Medium (DMEM) supplemented with 10% fetal bovine serum (FBS), 2 mM L-glutamine, 100 units of penicillin/mL and 100 µg/mL of streptomycin. All reagents were purchased from GIBCO. Cells were maintained in an incubator at 37ºC in a humidified atmosphere of 95% air and 5% CO_2.

Nanowires synthesis and characterization: The core-shell NWs composed of Fe were fabricated by electrochemical deposition into nanoporous alumina membranes, as previously reported.[96-98] The NWs' length was controlled by the deposition time, which was 1.5 h. The template containing the NWs was dissolved with 1 M sodium hydroxide, and the alumina membrane was removed. The sodium hydroxide solution was replaced every hour for four times. The NWs were then collected with a magnetic rack (DynaMag™-2; Life Technologies, Carlsbad, CA, USA) and rinsed thoroughly several times with ethanol with sonication steps in-between. The released NW´s were suspended in 1 mL of absolute ethanol and stored at room temperature. The morphology, length, and diameter of the NWs were investigated by SEM (Quanta 3D; FEI Company, Hillsboro, OR, USA) and TEM (Tecnai BioTWIN; FEI Company). The images were analyzed using ImageJ software as previously described.[49] The NWs' dimensions (i.e., length and thickness) were determined out of 100 NWs from different samples. Magnetization loops of NWs composed of Fe inside the alumina membrane were measured at room temperature with a vibrating sample magnetometer (Micro-Mag™ 3900, Lake Shore Cryotonics Inc., Westerville, OH). The alumina template with the embedded NWs was aligned parallel and perpendicular to the magnetic field applied. Measurements were performed by triplicate and expressed as average values. A sample of NWs was subjected to an oxidation process, where the NWs were first dried and then placed in an oven at 150°C overnight. The chemical composition of the NWs was investigated by scanning transmission electron microscopy (STEM) and EELS (Thermofisher (FEI) Titan Cube 80-300). The EELS maps were acquired in STEM mode as so-called spectrum imaging from 4 individual NWs. For sample preparation, 2µl of NWs suspended in absolute ethanol (0.2ug/ml) were added on a copper-carbon mesh substrate and left to dry before the examination.

Optical characterization of iron nanowires: The optical absorbance profile of two different samples of core-shell NWs composed of Fe in aqueous solution (0.05 mg Fe/ml) were determined in a Shimadzu UV-3600 Spectrophotometer. Measurements were performed in the optical range from 400 to 1300 nm in 1 cm path length cuvettes. A cuvette filled with miliQ water was used as a reference. Finite element method simulations of the Fe-based NWs was performed with COMSOL Multiphysics software and the model was based on the electromagnetic waves (frequency domain) module using Drude-Lorentz dispersion model for the metallic part (i.e. Fe) and relative permittivity model for the semiconductor part (i.e. the Fe_xO_y) and the surrounding media (i.e. air).

Photothermal efficiency of iron nanowires: The optical set-up used to trigger the photothermal effect of the core-shell NWs used a NIR 808 nm diode laser (Lumics, LU0808T040) as the illumination source with an irradiance of 0.8 W/cm^2. The laser beam was conducted through an optical fiber to the sample. The temperature was monitored using an infrared thermal camera (FLIR A35). In order to determine the efficiency of the core-shell NWs for photothermal applications, solutions of NWs in PBS with concentrations of 0.02, 0.04, and 0.2 mg Fe/mL were prepared. 110 µL of each solution was added into a quartz micro-cuvette (Cuvette Ultra Micro Cell, Hellma™), which was then irradiated with a NIR laser for 10 min. Special care was taken in order to guarantee that the full sample area was evenly illuminated. The temperature of the solution was monitored during irradiation and for 10 min after the laser was turned off. The camera was located on top of the sample to take thermal images directly from the solution´s surface. Thermographic images were collected from each solution at the point of maximum temperature, and a PBS solution without NWs was used as a negative control and for background correction. Temperature measurements were expressed as the change in the solution´s temperature over time. The photothermal response of the NWs after multiple irradiation cycles was evaluated by measuring the temperature of a solution of NWs in PBS (0.2 mg Fe/mL) before and after 10 min of laser irradiation for 5 consecutive days. The temperature delta at each irradiation cycle was normalized to the first measurement.

The photothermal conversion efficiency of the core-shell NWs was calculated as described by Roper et al.,[26] and adapted by Cole et al.,[27] where the following energy balance equation can be used to describe the change of temperature of the sample over time during and after the irradiation with the NIR laser.

$$\sum_i m_i C_{p,i} \frac{dT}{dt} = Q_I + Q_O + Q_{ext}, \quad (1)$$

where m_i and $C_{p,i}$ are the masses and heat capacities of each component i of the sample, $\frac{dT}{dt}$ is the change of the sample temperature T as a function of time t, Q_I is the energy input of the NWs, due to illumination, Q_0 is the energy input from the sample in the absence of NWs, *i.e.* the contribution of the solvent and the cuvette, and Q_{ext} is the outgoing energy. A model, in which Q_{ext} is linearly proportional to the temperature, is used with a heat transfer coefficient (h) as the proportionality constant

$$Q_{ext} = hA(T - T_{amb}), \quad (2)$$

where T_{amb} is the ambient temperature and A is the surface area of the sample. When the sample reaches an equilibrium temperature ($\frac{dT}{dt} = 0$), the energy flowing into the sample becomes equivalent to the energy outflow and from Equation (1) and (2),

$$Q_I + Q_O = hA(T_{max} - T_{amb}), \quad (3)$$

where T_{max} is the equilibrium temperature. Q_I is proportional to the energy absorbed by the NWs and depends thus on the illumination conditions and on the photothermal transduction efficiency (η) defined as the ratio of the heat energy produced by the NWs to the energy of the incident laser

$$Q_I = I(1 - 10^{-A\lambda})\eta \rightarrow \eta = \frac{hA(T_{max} - T_{amb}) - Q_O}{I(1 - 10^{-A\lambda})}, \quad (4)$$

where I is the power of the incident laser radiation and A_λ is the optical density of the sample solution at the laser wavelength used (808 nm). In the second term of Equation (4), Equation (3) has been used, and the resulting expression has been rearranged to give a definition of η in which almost every parameter can be easily determined experimentally. Indeed, only *h* remains unknown. However, within this model, a time constant (τ) can be introduced to describe the thermal evolution over time that would be given by

$$\tau = \frac{\sum_i m_i C_{p,i}}{h\mathrm{A}}, \quad (5)$$

From the cooling part of the temporal response curve, the thermal evolution behaves as a simple exponential decay with τ as time constant. Thus, the cooling curve can be fitted to experimentally determine *hA.* Additionally, the SLP was calculated from the temperature response curves of each NW solution by using the following expression:

$$SLP = \sum \frac{C_i m_i}{m_{Fe}} \frac{dT}{dt}\Big|_{max}, \quad (6)$$

where C_i is the specific heat capacity of each component of the solution, m_i is the mass of each component of the solution, m_{Fe} is the mass of NWs employed, and $\frac{dT}{dt}|_{max}$ is the slope of the temperature response immediately after starting with NIR irradiation of the sample. A linear fit was performed from the temperature response curves of aqueous suspensions with different concentration of NWs (see Supporting Information).

Functionalization and quantification of nanowires: NWs were functionalized following the previously described methodologies.[50, 56] The NWs were first coated with BSA. The surface charge, ζ (zeta) potential, of the NWs coated with BSA was measured in deionized (DI) water using a Zetasizer Nano ZS, He–Ne laser 633 nm (Malvern Instruments, Malvern, UK, n = 3). Coated NWs were then functionalized with a DOX derivative in and, from the functionalization supernatant, the covalently immobilized DOX onto thiolated NWs was indirectly determined by quantification of free DOX in solution (λmax = 495 nm) by UV/Vis spectrophotometry comparing the result with the result obtained from a solution of free DOX at the same concentration. All functionalization processes were carried out under sterile conditions and the DOX solution used was filtered through a 0.22-μm strainer. In order to quantify the amount of NWs contained in the NW solutions that are added to the seeded cells and the NWs that interact with the incubated cells, ICP-MS) for Fe quantification was performed (n = 3).

Confocal microscopy: The internalization of the core-shell NWs coated with BSA in MDA-MB-231 breast cancer cells was assessed using confocal reflection microscopy. Ibidi μ-slides 8 wells, seeded with $1x10^4$ cells/well and incubated for 24 h in 200 μL of DMEM containing 10% FBS for 24 h at 37°C and 5% CO_2 to reach confluence. The cells were treated with the NW concentrations 0.01 mg Fe/mL and 0.02 mg Fe/mL and incubated for 24 h at 37°C. Then, the cells were incubated for 30 min with NucRed™ Live 647 (ThermoFisher) (Figure 4 and Figure S6) or with DAPI (Figure S7), washed three times with PBS to remove free NWs, and, finally, 250 μL of Opti-MEM medium was added to each well. Cellular uptake was detected with a confocal laser scanning microscope (LSM 880, Carl Zeiss Jena, German) using a confocal reflection mode. Fixed excitation wavelengths of 633 nm and 488 nm were used for all the confocal fluorescent microscopy experiments for the cell nucleus observation and the NW detection by the reflection mode, respectively. Intracellular, focal plane-independent images, as well as intracellular z-stacks, were taken from samples incubated for 24, 48 and 72 h with the NW formulations. Experiments were performed by triplicate.

Photothermal effect of iron nanowires in cells: The potential of the core-shell NWs for photothermal therapy was evaluated in vitro in breast cancer cells. $6x10^4$ MDA-MB-231 breast cancer cells per well were seeded in a 24 well plate and incubated for 24 h to reach 90% confluence at 37ºC and 5% CO_2. Then, 0.02 mg Fe/mL BSA coated NWs were added to the cells and incubated for 24 h at 37ºC, 5% CO_2. The cells were washed twice with PBS and incubated for 10 min with 500 µL of trypsin at 37ºC. Unattached cells from 24 wells ($1.5x10^6$ cells) were collected in Eppendorf tubes, centrifuged at 10000 rpm for 20 min and the supernatant discarded carefully without drying the pellet, which was then solvated in 100 µL of PBS. A second pellet of non-treated cells (without NWs) was also formed and used as a negative control ($1.5x10^6$ cells). The complete volume of both cell solutions (200 µL) was placed into a 96 well plate, which was then irradiated with a NIR laser (808 nm) with a power density of 0.8 W/cm^2 for 10 min. The temperature was monitored every second during the irradiation time and for 5 min after the laser was turned off. The camera was located on top of the sample. Images were collected from each concentrated cell solution once the maximum temperature was reached. The results were expressed as the change in the temperature of the solution over time. The SLP of cells with internalized NWs was calculated by using the following expression:

$$SLP = \frac{(C_{PBS}m_{PBS} + C_{cell}m_{cell} + C_{Fe}m_{Fe})}{m_{Fe}}\frac{dT}{dt}\Big|_{max}, \quad (7)$$

where $C_{PBS}m_{PBS}$ are the mass and specific heat capacity of the PBS, $C_{cell}m_{cell}$ are the mass and specific heat capacity of the breast cancer cells, $C_{Fe}m_{Fe}$ are the mass and specific heat capacity of the Fe NWs employed, and $\frac{dT}{dt}|_{max}$ is the slope of the temperature response immediately after starting with NIR irradiation of the sample. A linear fit was performed from the temperature response curve of breast cancer cells with internalized NWs (see Supporting Information).

Combinatorial treatment and cell viability assays: To assess the cell death induction by various NW treatments, i.e.: NWs_DOX with and without AMF, with and without NIR laser irradiation as well as with and without AMF and combined with NIR laser irradiation, MDA-MB-231 cells were cultured on a 4-well plate at a density of $6x10^4$ cells per well in 500 µl of DMEM containing 10% FBS at 37°C and 5% CO_2 to reach 90% confluence. After 24 h, the growth medium was removed, and the cells were incubated for 24 h at 37°C with free DOX (1 µM), BSA coated NWs (0.02 mg Fe/mL), and NWs_DOX (0.02 mg Fe/mL, 1 µM of DOX). The concentration of the NWs tested in this experiment was found by ICP-MS from the NWs' stock solutions of both formulations, as previously described. As controls, non-treated cells and empty wells were used. After incubation, cells were washed three times with PBS and then maintained in 0.5 mL of DMEM containing 10% FBS at 37°C and 5% CO_2. Then, the magnetic field was applied for 10 min, while maintaining the temperature at 37°C. The AMF generator employed in this study was a home-made air-cooled ferrite core with a C shape and a gap of 16 mm, coiled with Litz wires. The AMF generator allows adjusting independently the frequency and intensity. The size of the core gap allowed applying the AMF to a single well of NUNC(TM) 4 well dishes (internal well diameter of 10 mm). The AMF direction was perpendicular to the wells, and its field intensity gradient was about 10% from the center of the well to the external border. Before the in vitro studies, it was experimentally confirmed that the AMF generator does not heat up the cell media under the conditions employed in this study. The applied AMF was 8 kA/m (field amplitude) and 10 Hz (field frequency). In order to investigate a possible heat generation by the NWs in the AMF, a solution of NWs in PBS (0.2 mg Fe/mL) was subjected to the AMF and the temperature recorded. Immediately after the magnetic treatment, NIR laser irradiation (808 nm, 0.8 W/cm^2) was applied for 10 min at 37°C. Cell viability was assessed using the Alamar Blue assay. After 72 h of post-treatment incubation, the medium was replaced with DMEM containing 10% FBS and 5% of Resazurin dye (1 mg/ml PBS). Cells were maintained at 37°C and 5% CO_2 in an incubator for 4 h, after which a Tecan GENiosPro multimode microplate reader was used to determine the amount of Resazurin by measuring the fluorescence of the supernatant (excitation 540 nm, emission 590 nm). 500 µl of 5% of Resazurin dye were added to empty wells as a negative control. The viability of the cells was expressed as the percentage of fluorescence of treated cells in comparison to control cells (untreated). All experiments were carried out in four sets of quadruplicates, one set with the AMF, one set with NIR irradiation, one with both AMF and NIR irradiation, and one without any of the treatments.

Statistical analysis: All the data obtained from the in vitro cell viability assays were plotted and statistically analyzed using the software package GraphPad Prism version 7 for Windows. All samples were compared using a one-way ANOVA and Tukey's multiple comparison test (*$P < 0.05$, **$P < 0.01$, and ***$P < 0.001$). Only significant differences among the samples are indicated in the chart.

ASSOCIATED CONTENT

The following files are available free of charge.

Additional Figures and Tables (PDF)

Supporting Videos

AUTHOR INFORMATION

Corresponding Author

* Jürgen Kosel

E-mail: jurgen.kosel@kaust.edu.sa

* Aitziber L. Cortajarena

E-mail: alcortajarena@cicbiomagune.es

Author Contributions

The manuscript was written through contributions of all authors. All authors have given approval to the final version of the manuscript. ‡These authors contributed equally.

Funding Sources

Research reported in this publication was supported by the King Abdullah University of Science and Technology (KAUST). This work has been partially funded by the Spanish Ministerio de Economía y Competitividad (BIO2016-77367-C2-1-R, SEV-2016-0686 and MAT2016-81955-REDT), the Basque Government (Elkartek KK-2017/00008), and Madrid Regional Government (PEJ-2017-AI/IND-6283). This work was performed under the Maria de Maeztu Units of Excellence Program from the Spanish State Research

Agency – Grant No. MDM-2017-0720 (CIC biomaGUNE). C.L.-P. acknowledges financial support from CAM (PEJ-2017-AI/IND-6283). A. I. M.-B. and A. A. contributed equally to this work.

Notes

The authors declare no competing financial interest..

ACKNOWLEDGMENT

We thank Irantzu llarena at CIC biomaGUNE for support with confocal microscopy measurements and Sergei Lopatin from the Imaging and Characterization Corel Lab at KAUST.

ABBREVIATIONS

NW(s) nanowire(s); NIR, near-infrared; AMF, alternating magnetic field; DOX, doxorubicin; BSA, bovine serum albumin; NWs_DOX, nanowires functionalized with doxorubicin; PBS, phosphate buffer saline; FBS, fetal bovine serum; DMEM, Dulbecco's modified eagle's medium; ICP-MS, inductively coupled plasma mass spectrometry; TEM, transmission electron microscopy, SEM, scanning electron microscopy; EELS, electron energy loss spectroscopy; Ms, saturation magnetization; Hc, coercivity; υ, frequency; SLP specific loss power; HDC, heat dose per cell.

REFERENCES

(1) Pasparakis, G.; Manouras, T.; Vamvakaki, M.; Argitis, P. Harnessing Photochemical Internalization with Dual Degradable Nanoparticles for Combinatorial Photo–Chemotherapy. *Nature Communications* **2014,** *5*, 3623.

(2) Li, Y.; Lin, T.-y.; Luo, Y.; Liu, Q.; Xiao, W.; Guo, W.; Lac, D.; Zhang, H.; Feng, C.; Wachsmann-Hogiu, S.; Walton, J. H.; Cherry, S. R.; Rowland, D. J.; Kukis, D.; Pan, C.; Lam, K. S. A Smart and Versatile Theranostic Nanomedicine Platform Based on Nanoporphyrin. *Nature Communications* **2014,** *5*, 4712.

(3) Di Corato, R.; Béalle, G.; Kolosnjaj-Tabi, J.; Espinosa, A.; Clément, O.; Silva, A. K. A.; Ménager, C.; Wilhelm, C. Combining Magnetic Hyperthermia and Photodynamic Therapy for Tumor Ablation with Photoresponsive Magnetic Liposomes. *ACS Nano* **2015,** *9*, 2904-2916.

(4) Faraji, A. H.; Wipf, P. Nanoparticles in Cellular Drug Delivery. *Bioorganic & Medicinal Chemistry* **2009,** *17*, 2950-2962.

(5) Swai, H.; Semete, B.; Kalombo, L.; Chelule, P.; Kisich, K.; Sievers, B. Nanomedicine for Respiratory Diseases. *Wiley Interdisciplinary Reviews-Nanomedicine and Nanobiotechnology* **2009,** *1*, 255-263.

(6) Banerjee, S. S.; Chen, D. H. Multifunctional Ph-Sensitive Magnetic Nanoparticles for Simultaneous Imaging, Sensing and Targeted Intracellular Anticancer Drug Delivery. *Nanotechnology* **2008,** *19*, 8.

(7) Othman, B. A.; Greenwood, C.; Abuelela, A. F.; Bharath, A. A.; Chen, S.; Theodorou, I.; Douglas, T.; Uchida, M.; Ryan, M.; Merzaban, J. S.; Porter, A. E. Correlative Light-Electron Microscopy Shows Rgd-Targeted Zno Nanoparticles Dissolve in the Intracellular

Environment of Triple Negative Breast Cancer Cells and Cause Apoptosis with Intratumor Heterogeneity. *Advanced Healthcare Materials* **2016,** *5*, 1310-1325.

(8) Kim, J. E.; Shin, J. Y.; Cho, M. H. Magnetic Nanoparticles: An Update of Application for Drug Delivery and Possible Toxic Effects. *Archives of Toxicology* **2012,** *86*, 685-700.

(9) Li, F.; Kosel, J. An Efficient Biosensor Made of an Electromagnetic Trap and a Magneto-Resistive Sensor. *Biosensors & bioelectronics* **2014,** *59*, 145-150.

(10) Yu, M. K.; Park, J.; Jon, S. Targeting Strategies for Multifunctional Nanoparticles in Cancer Imaging and Therapy. *Theranostics* **2012,** *2*, 3-44.

(11) Holligan, D. L.; Gillies, G. T.; Dailey, J. P. Magnetic Guidance of Ferrofluidic Nanoparticles in an in Vitro Model of Intraocular Retinal Repair. *Nanotechnology* **2003,** *14*, 661.

(12) Keshoju, K.; Xing, H.; Sun, L. Magnetic Field Driven Nanowire Rotation in Suspension. *Applied Physics Letters* **2007,** *91*, 3.

(13) Wei-Syuan, L.; Hong-Ming, L.; Hsiang-Hsin, C.; Yeu-Kuang, H.; Yuh-Jing, C. Shape Effects of Iron Nanowires on Hyperthermia Treatment. *Journal of Nanomaterials* **2013,** *2013*.

(14) Grile, G. The Effects of Heat and Radiation on Cancers Implanted on the Feet of Mice. *Cancer Res.* **1963,** *23*, 372.

(15) Kossatz, S.; Grandke, J.; Couleaud, P.; Latorre, A.; Aires, A.; Crosbie-Staunton, K.; Ludwig, R.; Daehring, H.; Ettelt, V.; Lazaro-Carrillo, A.; Calero, M.; Sader, M.; Courty, J.; Volkov, Y.; Prina-Mello, A.; Villanueva, A.; Somoza, A.; Cortajarena, A. L.; Miranda, R.; Hilger, I. Efficient Treatment of Breast Cancer Xenografts with Multifunctionalized Iron Oxide Nanoparticles Combining Magnetic Hyperthermia and Anti-Cancer Drug Delivery. *Breast Cancer Research* **2015,** *17*.

(16) Jordan, A.; Scholz, R.; Wust, P.; Fähling, H.; Roland, F. Magnetic Fluid Hyperthermia (Mfh): Cancer Treatment with Ac Magnetic Field Induced Excitation of Biocompatible Superparamagnetic Nanoparticles. *Journal of Magnetism and Magnetic Materials* **1999,** *201*, 413-419.

(17) Hogan, N. J.; Urban, A. S.; Ayala-Orozco, C.; Pimpinelli, A.; Nordlander, P.; Halas, N. J. Nanoparticles Heat through Light Localization. *Nano Letters* **2014,** *14*, 4640-4645.

(18) Huang, X.; El-Sayed, I. H.; Qian, W.; El-Sayed, M. A. Cancer Cell Imaging and Photothermal Therapy in the near-Infrared Region by Using Gold Nanorods. *Journal of the American Chemical Society* **2006,** *128*, 2115-2120.

(19) Huang, X.; Jain, P. K.; El-Sayed, I. H.; El-Sayed, M. A. J. L. i. M. S. Plasmonic Photothermal Therapy (Pptt) Using Gold Nanoparticles. **2007,** *23*, 217.

(20) Boca, S. C.; Potara, M.; Gabudean, A.-M.; Juhem, A.; Baldeck, P. L.; Astilean, S. Chitosan-Coated Triangular Silver Nanoparticles as a Novel Class of Biocompatible, Highly Effective Photothermal Transducers for in Vitro Cancer Cell Therapy. *Cancer Letters* **2011,** *311*, 131-140.

(21) Zhou, M.; Zhang, R.; Huang, M.; Lu, W.; Song, S.; Melancon, M. P.; Tian, M.; Liang, D.; Li, C. A Chelator-Free Multifunctional [64cu]Cus Nanoparticle Platform for Simultaneous Micro-Pet/Ct Imaging and Photothermal Ablation Therapy. *Journal of the American Chemical Society* **2010,** *132*, 15351-15358.

(22) Loo, C.; Lowery, A.; Halas, N.; West, J.; Drezek, R. Immunotargeted Nanoshells for Integrated Cancer Imaging and Therapy. *Nano Letters* **2005,** *5*, 709-711.

(23) Moon, H. K.; Lee, S. H.; Choi, H. C. In Vivo near-Infrared Mediated Tumor Destruction by Photothermal Effect of Carbon Nanotubes. *ACS Nano* **2009,** *3*, 3707-3713.

(24) Wang, Y.-H.; Chen, S.-P.; Liao, A.-H.; Yang, Y.-C.; Lee, C.-R.; Wu, C.-H.; Wu, P.-C.; Liu, T.-M.; Wang, C.-R. C.; Li, P.-C. Synergistic Delivery of Gold Nanorods Using Multifunctional Microbubbles for Enhanced Plasmonic Photothermal Therapy. *Scientific Reports* **2014,** *4*, 5685.

(25) Savchuk, O. A.; Carvajal, J. J.; Massons, J.; Aguiló, M.; Díaz, F. Determination of Photothermal Conversion Efficiency of Graphene and Graphene Oxide through an Integrating Sphere Method. *Carbon* **2016,** *103*, 134-141.

(26) Roper, D. K.; Ahn, W.; Hoepfner, M. Microscale Heat Transfer Transduced by Surface Plasmon Resonant Gold Nanoparticles. *J. Phys. Chem. C* **2007,** *111*, 3636-3641.

(27) Cole, J. R.; Mirin, N. A.; Knight, M. W.; Goodrich, G. P.; Halas, N. J. Photothermal Efficiencies of Nanoshells and Nanorods for Clinical Therapeutic Applications. *J. Phys. Chem. C* **2009,** *113*, 12090-12094.

(28) Maestro, L. M.; Haro-González, P.; Sánchez-Iglesias, A.; Liz-Marzán, L. M.; García Solé, J.; Jaque, D. Quantum Dot Thermometry Evaluation of Geometry Dependent Heating Efficiency in Gold Nanoparticles. *Langmuir* **2014,** *30*, 1650-1658.

(29) Thiesen, B.; Jordan, A. Clinical Applications of Magnetic Nanoparticles for Hyperthermia. *International Journal of Hyperthermia* **2008,** *24*, 467-474.

(30) Johannsen, M.; Thiesen, B.; Wust, P.; Jordan, A. Magnetic Nanoparticle Hyperthermia for Prostate Cancer. *International Journal of Hyperthermia* **2010,** *26*, 790-795.

(31) Maier-Hauff, K.; Ulrich, F.; Nestler, D.; Niehoff, H.; Wust, P.; Thiesen, B.; Orawa, H.; Budach, V.; Jordan, A. Efficacy and Safety of Intratumoral Thermotherapy Using Magnetic Iron-Oxide Nanoparticles Combined with External Beam Radiotherapy on

Patients with Recurrent Glioblastoma Multiforme. *Journal of Neuro-Oncology* **2011,** *103*, 317-324.

(32) Lartigue, L.; Alloyeau, D.; Kolosnjaj-Tabi, J.; Javed, Y.; Guardia, P.; Riedinger, A.; Péchoux, C.; Pellegrino, T.; Wilhelm, C.; Gazeau, F. Biodegradation of Iron Oxide Nanocubes: High-Resolution in Situ Monitoring. *ACS Nano* **2013,** *7*, 3939-3952.

(33) Feliu, N.; Docter, D.; Heine, M.; del Pino, P.; Ashraf, S.; Kolosnjaj-Tabi, J.; Macchiarini, P.; Nielsen, P.; Alloyeau, D.; Gazeau, F.; Stauber, R. H.; Parak, W. J. In Vivo Degeneration and the Fate of Inorganic Nanoparticles. *Chemical Society Reviews* **2016,** *45*, 2440-2457.

(34) Volatron, J.; Carn, F.; Kolosnjaj-Tabi, J.; Javed, Y.; Vuong, Q. L.; Gossuin, Y.; Ménager, C.; Luciani, N.; Charron, G.; Hémadi, M.; Alloyeau, D.; Gazeau, F. Ferritin Protein Regulates the Degradation of Iron Oxide Nanoparticles. *Small* **2017,** *13*, 1602030.

(35) Gutiérrez, L.; Romero, S.; da Silva Gustavo, B.; Costo, R.; Vargas Maria, D.; Ronconi Célia, M.; Serna Carlos, J.; Veintemillas-Verdaguer, S.; del Puerto Morales, M.,

Degradation of Magnetic Nanoparticles Mimicking Lysosomal Conditions Followed by Ac Susceptibility. In *Biomedical Engineering / Biomedizinische Technik*, 2015; Vol. 60, p 417.

(36) Yi, Z.; Hansong, Z. Rotational Maneuver of Ferromagnetic Nanowires for Cell Manipulation. *IEEE Transactions on Nanobioscience* **2009,** *8*, 226-236.

(37) Shore, D.; Pailloux, S. L.; Zhang, J.; Gage, T.; Flannigan, D. J.; Garwood, M.; Pierre, V. C.; Stadler, B. J. H. Electrodeposited Fe and Fe-Au Nanowires as Mri Contrast Agents. *Chem. Commun.* **2016,** *52*, 12634-12637.

(38) Korchinski, D. J.; Taha, M.; Yang, R.; Nathoo, N.; Dunn, J. F. Iron Oxide as an Mri Contrast Agent for Cell Tracking. *Magnetic Resonance Insights* **2015,** *8*, 15-29.

(39) Hilger, I.; Kaiser, W. A. Iron Oxide-Based Nanostructures for Mri and Magnetic Hyperthermia. *Nanomedicine* **2012,** *7*, 1443-1459.

(40) Zhou, Z.; Sun, Y.; Shen, J.; Wei, J.; Yu, C.; Kong, B.; Liu, W.; Yang, H.; Yang, S.; Wang, W. Iron/Iron Oxide Core/Shell Nanoparticles for Magnetic Targeting Mri and near-Infrared Photothermal Therapy. *Biomaterials* **2014,** *35*, 7470-7478.

(41) Shen, S.; Kong, F.; Guo, X.; Wu, L.; Shen, H.; Xie, M.; Wang, X.; Jin, Y.; Ge, Y. Cmcts Stabilized Fe3o4 Particles with Extremely Low Toxicity as Highly Efficient near-Infrared Photothermal Agents for in Vivo Tumor Ablation. *Nanoscale* **2013,** *5*, 8056-8066.

(42) Chen, H.; Burnett, J.; Zhang, F.; Zhang, J.; Paholak, H.; Sun, D. Highly Crystallized Iron Oxide Nanoparticles as Effective and Biodegradable Mediators for Photothermal Cancer Therapy. *Journal of Materials Chemistry B* **2014,** *2*, 757-765.

(43) Shen, S.; Wang, S.; Zheng, R.; Zhu, X.; Jiang, X.; Fu, D.; Yang, W. Magnetic Nanoparticle Clusters for Photothermal Therapy with near-Infrared Irradiation. *Biomaterials* **2015,** *39*, 67-74.

(44) Espinosa, A.; Di Corato, R.; Kolosnjaj-Tabi, J.; Flaud, P.; Pellegrino, T.; Wilhelm, C. Duality of Iron Oxide Nanoparticles in Cancer Therapy: Amplification of Heating Efficiency by Magnetic Hyperthermia and Photothermal Bimodal Treatment. *Acs Nano* **2016,** *10*, 2436-2446.

(45) Hanan, M.; Julian, A. M.; Jürgen, K. Advanced Fabrication and Characterization of Magnetic Nanowires. **2018**.

(46) Meng-Meng, S.; Wen-Jing, S.; Hong, B.; Jun, W.; Wei-Lin, W.; Jun, S.; Min, Y. Cytotoxicity and Cellular Uptake of Iron Nanowires. *Biomaterials* **2010,** *31*, 1509-1517.

(47) Contreras, M. F.; Sougrat, R.; Zaher, A.; Ravasi, T.; Kosel, J. Non-Chemotoxic Induction of Cancer Cell Death Using Magnetic Nanowires. *Int. J. Nanomed.* **2015,** *10*, 2141-2153.

(48) Hultgren, A.; Tanase, M.; Felton, E. J.; Bhadriraju, K.; Salem, A. K.; Chen, C. S.; Reich, D. H. Optimization of Yield in Magnetic Cell Separations Using Nickel Nanowires of Different Lengths. *Biotechnology Progress* **2005,** *21*, 509-515.

(49) Perez, J. E.; Contreras, M. F.; Vilanova, E.; Felix, L. P.; Margineanu, M. B.; Luongo, G.; Porter, A. E.; Dunlop, I. E.; Ravasi, T.; Kosel, J. Cytotoxicity and Intracellular Dissolution of Nickel Nanowires. *Nanotoxicology* **2015**, 1-10.

(50) Martínez-Banderas, A. I.; Aires, A.; Teran, F. J.; Perez, J. E.; Cadenas, J. F.; Alsharif, N.; Ravasi, T.; Cortajarena, A. L.; Kosel, J. Functionalized Magnetic Nanowires for Chemical and Magneto-Mechanical Induction of Cancer Cell Death. *Sci. Rep.* **2016,** *6*, 35786.

(51) Gunnar, G.; Rudolf, H.; Matthias, Z.; Silvio, D.; Stefan, N.; Werner, W. The Effect of Field Parameters, Nanoparticle Properties and Immobilization on the Specific Heating Power in Magnetic Particle Hyperthermia. *Journal of Physics: Condensed Matter* **2006,** *18*, S2935.

(52) Rudolf, H.; Silvio, D.; Robert, M.; Matthias, Z. Magnetic Particle Hyperthermia: Nanoparticle Magnetism and Materials Development for Cancer Therapy. *Journal of Physics: Condensed Matter* **2006,** *18*, S2919.

(53) Ivanov, Y. P.; Alfadhel, A.; Alnassar, M.; Perez, J. E.; Vazquez, M.; Chuvilin, A.; Kosel, J. Tunable Magnetic Nanowires for Biomedical and Harsh Environment Applications. *Scientific Reports* **2016,** *6*, 24189.

(54) Reich, D. H.; Tanase, M.; Hultgren, A.; Bauer, L. A.; Chen, C. S.; Meyer, G. J. Biological Applications of Multifunctional Magnetic Nanowires (Invited). *Journal of Applied Physics* **2003,** *93*, 7275-7280.

(55) Alfadhel, A.; Kosel, J. Magnetic Nanocomposite Cilia Tactile Sensor. *Advanced Materials* **2015,** *27*, 7888-7892.

(56) Aires, A.; Ocampo, S. M.; Cabrera, D.; de la Cueva, L.; Salas, G.; Teran, F. J.; Cortajarena, A. L. Bsa-Coated Magnetic Nanoparticles for Improved Therapeutic Properties. *Journal of Materials Chemistry B* **2015,** *3*, 6239-6247.

(57) Margineanu, M. B.; Julfakyan, K.; Sommer, C.; Perez, J. E.; Contreras, M. F.; Khashab, N.; Kosel, J.; Ravasi, T. Semi-Automated Quantification of Living Cells with Internalized Nanostructures. *Journal of Nanobiotechnology* **2016,** *14*, 13.

(58) Alsharif, N. A.; Martinez-Banderas, A.; Merzaban, J.; Ravasi, T.; Kosel, J. Biofunctionalizing Magnetic Nanowires toward Targeting and Killing Leukemia Cancer Cells. *IEEE Transactions on Magnetics* **2019,** *55*, 1-5.

(59) Willner, D.; Trail, P. A.; Hofstead, S. J.; King, H. D.; Lasch, S. J.; Braslawsky, G. R.; Greenfield, R. S.; Kaneko, T.; Firestone, R. A. (6-Maleimidocaproyl)Hydrazone of Doxorubicin - a New Derivative for the Preparation of Immunoconjugates of Doxorubicin. *Bioconjugate Chemistry* **1993,** *4*, 521-527.

(60) Miao, G.; Yu, Y.; Xiaozhou, L.; Husheng, Y.; Keliang, L.; Hongkai, Z.; Youjia, C. Multilayer Nanoparticles with a Magnetite Core and a Polycation Inner Shell as Ph-Responsive Carriers for Drug Delivery. *Nanoscale* **2010,** *2*, 434-441.

(61) Tojkander, S.; Gateva, G.; Lappalainen, P. Actin Stress Fibers – Assembly, Dynamics and Biological Roles. *Journal of Cell Science* **2012,** *125*, 1855.

(62) Tang, J.; Myers, M.; Bosnick, K. A.; Brus, L. E. Magnetite Fe3o4 Nanocrystals: Spectroscopic Observation of Aqueous Oxidation Kinetics. *The Journal of Physical Chemistry B* **2003,** *107*, 7501-7506.

(63) He, Y. P.; Miao, Y. M.; Li, C. R.; Wang, S. Q.; Cao, L.; Xie, S. S.; Yang, G. Z.; Zou, B. S.; Burda, C. Size and Structure Effect on Optical Transitions of Iron Oxide Nanocrystals. *Physical Review B* **2005,** *71*, 125411.

(64) Alafano, R. R.; Demos, S. G.; Gayen, S. K. Advances in Optical Imaging of Biomedical Mediaa. *Annals of the New York Academy of Sciences* **1997,** *820*, 248-271.

(65) Guo, L.; Huang, Q.; Li, X.-y.; Yang, S. Iron Nanoparticles: Synthesis and Applications in Surface Enhanced Raman Scattering and Electrocatalysis. *Physical Chemistry Chemical Physics* **2001,** *3*, 1661-1665.

(66) Corliss, C.; Sugar, J. Energy Levels of Iron, Fe I through Fe Xxvi. *Journal of Physical and Chemical Reference Data* **1982,** *11*, 135-241.

(67) Michaelson, H. B. The Work Function of the Elements and Its Periodicity. *Journal of Applied Physics* **1977,** *48*, 4729-4733.

(68) Griffiths, D. J. *Introduction to Electrodynamics*, Fourth edition. Boston : Pearson, [2013] ©2013: 2013.

(69) Webb, J. A.; Bardhan, R. Emerging Advances in Nanomedicine with Engineered Gold Nanostructures. *Nanoscale* **2014,** *6*, 2502-2530.

(70) Williams, R. K.; Yarbrough, D. W.; Masey, J. W.; Holder, T. K.; Graves, R. S. Experimental Determination of the Phonon and Electron Components of the Thermal Conductivity of Bcc Iron. *Journal of Applied Physics* **1981,** *52*, 5167-5175.

(71) Mo/lgaard, J.; Smeltzer, W. W. Thermal Conductivity of Magnetite and Hematite. *Journal of Applied Physics* **1971,** *42*, 3644-3647.

(72) Hua, B.; Lin, Q.; Zhang, Q.; Fan, Z. Efficient Photon Management with Nanostructures for Photovoltaics. *Nanoscale* **2013,** *5*, 6627-6640.

(73) Ai, Z.; Gao, Z.; Zhang, L.; He, W.; Yin, J. J. Core–Shell Structure Dependent Reactivity of Fe@Fe2o3 Nanowires on Aerobic Degradation of 4-Chlorophenol. *Environmental Science & Technology* **2013,** *47*, 5344-5352.

(74) Clavero, C. Plasmon-Induced Hot-Electron Generation at Nanoparticle/Metal-Oxide Interfaces for Photovoltaic and Photocatalytic Devices. *Nature Photonics* **2014,** *8*, 95.

(75) Sadat, M. E.; Baghbador, M. K.; Dunn, A. W.; Wagner, H. P.; Ewing, R. C.; Zhang, J.; Xu, H.; Pauletti, G. M.; Mast, D. B.; Shi, D. Photoluminescence and Photothermal Effect of Fe3o4 Nanoparticles for Medical Imaging and Therapy. *Applied Physics Letters* **2014,** *105*, 091903.

(76) Mann, S. A.; Garnett, E. C. Extreme Light Absorption in Thin Semiconductor Films Wrapped around Metal Nanowires. *Nano Letters* **2013,** *13*, 3173-3178.

(77) Querry, M. R. *Optical Constants*, Contractor report, US Army Chemical Research, Development and Engineering Center (CRDC): Aberdeen Proving Ground, MD, USA, 1985.

(78) Lazareva, E. N.; Tuchin, V. V. Blood Refractive Index Modelling in the Visible and near Infrared Spectral Regions. *2018* **2018,** *4*.

(79) Ding, H.; Lu, J. Q.; Wooden, W. A.; Kragel, P. J.; Hu, X.-H. Refractive Indices of Human Skin Tissues at Eight Wavelengths and Estimated Dispersion Relations between 300 and 1600 Nm. *Physics in Medicine and Biology* **2006,** *51*, 1479-1489.

(80) Natividad, E.; Castro, M.; Mediano, A. Accurate Measurement of the Specific Absorption Rate Using a Suitable Adiabatic Magnetothermal Setup. *Applied Physics Letters* **2008,** *92*, 093116.

(81) Wang, S.; Huang, S.; Borca-Tasciuc, D. Potential Sources of Errors in Measuring and Evaluating the Specific Loss Power of Magnetic Nanoparticles in an Alternating Magnetic Field. *IEEE Transactions on Magnetics* **2013,** *49*, 255-262.

(82) Wildeboer, R. R.; Southern, P.; Pankhurst, Q. A. On the Reliable Measurement of Specific Absorption Rates and Intrinsic Loss Parameters in Magnetic Hyperthermia Materials. *Journal of Physics D: Applied Physics* **2014,** *47*, 495003.

(83) Cabrera, D.; Rubia-Rodríguez, I.; Garaio, E.; Plazaola, F.; Dupré, L.; Farrow, N.; Teran, F. J.; Ortega, D. Instrumentation for Magnetic Hyperthermia. In *Nanomaterials for Magnetic and Optical Hyperthermia Applications*; Fratila, R.; De La Fuente, J. M., Eds.; Elsevier: 2018.

(84) Gonzales-Weimuller, M.; Zeisberger, M.; Krishnan, K. M. Size-Dependant Heating Rates of Iron Oxide Nanoparticles for Magnetic Fluid Hyperthermia. *Journal of Magnetism and Magnetic Materials* **2009,** *321*, 1947-1950.

(85) Guardia, P.; Di Corato, R.; Lartigue, L.; Wilhelm, C.; Espinosa, A.; Garcia-Hernandez, M.; Gazeau, F.; Manna, L.; Pellegrino, T. Water-Soluble Iron Oxide

Nanocubes with High Values of Specific Absorption Rate for Cancer Cell Hyperthermia Treatment. *ACS Nano* **2012,** *6*, 3080-3091.

(86) Martinez-Boubeta, C.; Simeonidis, K.; Makridis, A.; Angelakeris, M.; Iglesias, O.; Guardia, P.; Cabot, A.; Yedra, L.; Estradé, S.; Peiró, F.; Saghi, Z.; Midgley, P. A.; Conde-Leborán, I.; Serantes, D.; Baldomir, D. Learning from Nature to Improve the Heat Generation of Iron-Oxide Nanoparticles for Magnetic Hyperthermia Applications. *Scientific Reports* **2013,** *3*, 1652.

(87) Lee, J.-H.; Jang, J.-t.; Choi, J.-s.; Moon, S. H.; Noh, S.-h.; Kim, J.-w.; Kim, J.-G.; Kim, I.-S.; Park, K. I.; Cheon, J. Exchange-Coupled Magnetic Nanoparticles for Efficient Heat Induction. *Nat. Nanotechnol.* **2011,** *6*, 418.

(88) Di Corato, R.; Espinosa, A.; Lartigue, L.; Tharaud, M.; Chat, S.; Pellegrino, T.; Ménager, C.; Gazeau, F.; Wilhelm, C. Magnetic Hyperthermia Efficiency in the Cellular Environment For different Nanoparticle Designs. *Biomaterials* **2014,** *35*, 6400-6411.

(89) Perez, J. E.; Contreras, M. F.; Vilanova, E.; Ravasi, T.; Kosel, J. Cytotoxicity and Effects on Cell Viability of Nickel Nanowires. *International Conference on Biological, Medical and Chemical Engineering (Bmce 2013)* **2013**, 178-184.

(90) Malak, S.; Yan, M. H.; Guedeau-Boudeville, M. A.; Conjeaud, H.; Garnier-Thibaud, V.; Boggetto, N.; Baeza-Squiban, A.; Niedergang, F.; Averbeck, D.; Berret, J. F. Interactions between Magnetic Nanowires and Living Cells: Uptake, Toxicity and Degradation. *Abstracts of Papers of the American Chemical Society* **2012,** *243*, 1.

(91) Perez, J. E.; Contreras, M. F.; Vilanova, E.; Felix, L. P.; Margineanu, M. B.; Luongo, G.; Porter, A. E.; Dunlop, I. E.; Ravasi, T.; Kosel, J. Cytotoxicity and Intracellular Dissolution of Nickel Nanowires. *Nanotoxicology* **2016,** *10*, 871-880.

(92) Schinwald, A.; Donaldson, K. Use of Back-Scatter Electron Signals to Visualise Cell/Nanowires Interactions in Vitro and in Vivo; Frustrated Phagocytosis of Long Fibres in Macrophages and Compartmentalisation in Mesothelial Cells in Vivo. *Particle and Fibre Toxicology* **2012,** *9*, 34.

(93) Engelmann, U. M.; Roeth, A. A.; Eberbeck, D.; Buhl, E. M.; Neumann, U. P.; Schmitz-Rode, T.; Slabu, I. Combining Bulk Temperature and Nanoheating Enables Advanced Magnetic Fluid Hyperthermia Efficacy on Pancreatic Tumor Cells. *Scientific Reports* **2018,** *8*, 13210.

(94) Latorre, A.; Couleaud, P.; Aires, A.; Cortajarena, A. L.; Somoza, A. Multifunctionalization of Magnetic Nanoparticles for Controlled Drug Release: A General Approach. *European Journal of Medicinal Chemistry* **2014,** *82*, 355-362.

(95) Da Silva, C. G.; Peters, G. J.; Ossendorp, F.; Cruz, L. J. J. C. C.; Pharmacology. The Potential of Multi-Compound Nanoparticles to Bypass Drug Resistance in Cancer. **2017,** *80*, 881-894.

(96) Nielsch, K.; Muller, F.; Li, A. P.; Gosele, U. Uniform Nickel Deposition into Ordered Alumina Pores by Pulsed Electrodeposition. *Adv Mater* **2000,** *12*, 582-586.

(97) Pirota, K. R.; Navas, D.; Hernandez-Velez, M.; Nielsch, K.; Vazquez, M. Novel Magnetic Materials Prepared by Electrodeposition Techniques: Arrays of Nanowires and Multi-Layered Microwires. *J. Alloys Compd.* **2004,** *369*, 18-26.

(98) Masuda, H.; Fukuda, K. Ordered Metal Nanohole Arrays Made by a 2-Step Replication of Honeycomb Structures of Anodic Alumina. *Science* **1995,** *268*, 1466-1468.

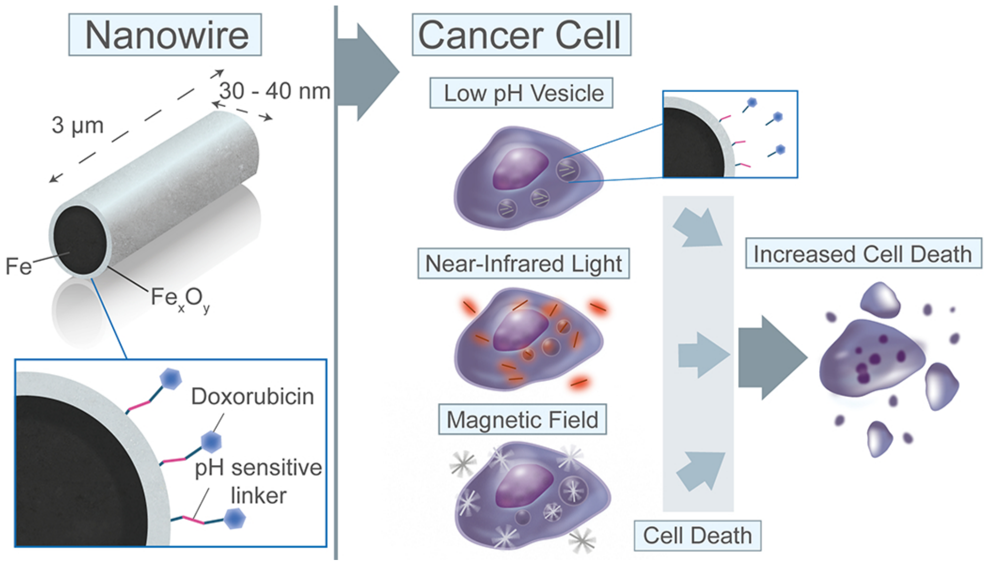
Nanowire
3 µm
30 - 40 nm
Fe
FexOy
Doxorubicin
pH sensitive
linker
Cancer Cell
Low pH Vesicle
Near-Infrared Light
Magnetic Field
Increased Cell Death
Cell Death

TOC

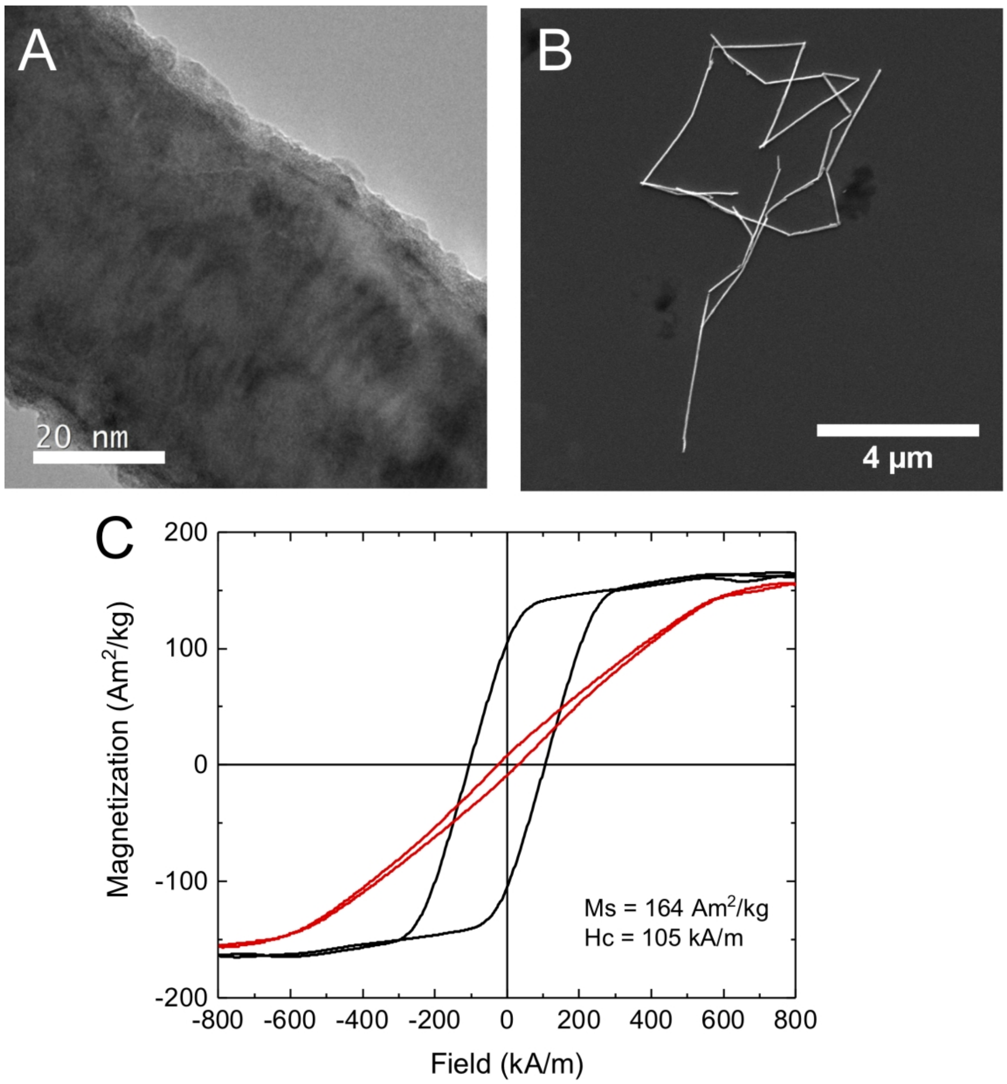

Figure 1. Characterization of Fe-FexOy core-shell NWs. (A) TEM image of a single NW. (B) SEM image of NWs on a silicon substrate after functionalization. (C) Magnetization curves of NWs embedded in the alumina membrane with the NWs placed parallel (black curve) and perpendicular (red curve) to the direction of the applied magnetic field (MS is the saturation magnetization and HC the coercive field, n = 3).

194x209mm (300 x 300 DPI)

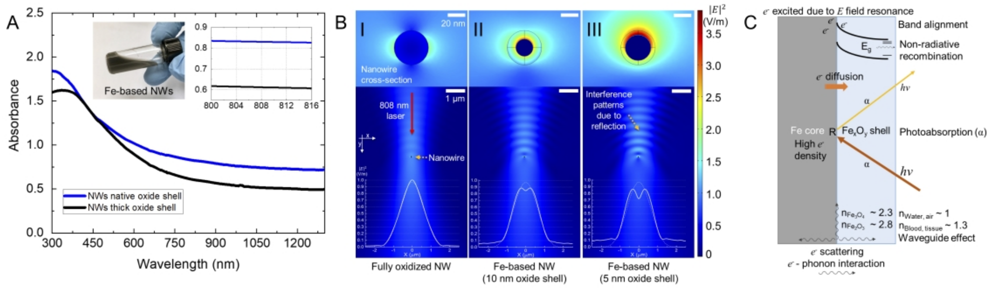

Figure 2. Optical characterization of Fe-FexOy core-shell NWs with different oxidation level. (A) Optical absorption spectra of aqueous solutions of Fe-FexOy core-shell NWs with native oxide layer (blue) and exposed to oxidizing conditions (black), both at the Fe concentration of 0.05 mg of Fe/mL. Insets show an aqueous solution of Fe NWs (left) and a magnification of the region of interest (right). (B) Simulation of the light absorption in NWs with different oxidation levels showing the intensity of electric field generated by the interaction of a focused laser light (808 nm) and the cross-section of the NWs. The top row shows the vicinity of the NWs and the bottom row shows the light path and intensity profile of the incident light after interaction with (BI) a fully oxidized NW, (BII) a model of the NW exposed to oxidizing conditions (FexOy shell = 10 nm), and (BIII) a model of the NW with native oxide shell (FexOy shell = 5 nm). For comparison, the electric field profile of the laser light without obstacles (i.e. without NWs) is plotted as dotted line. (C) Proposed phenomena of the light-matter interaction for Fe-FexOy core-shell NWs upon light exposure, leading to increased light absorption and augmented photothermal effect.

597x172mm (300 x 300 DPI)

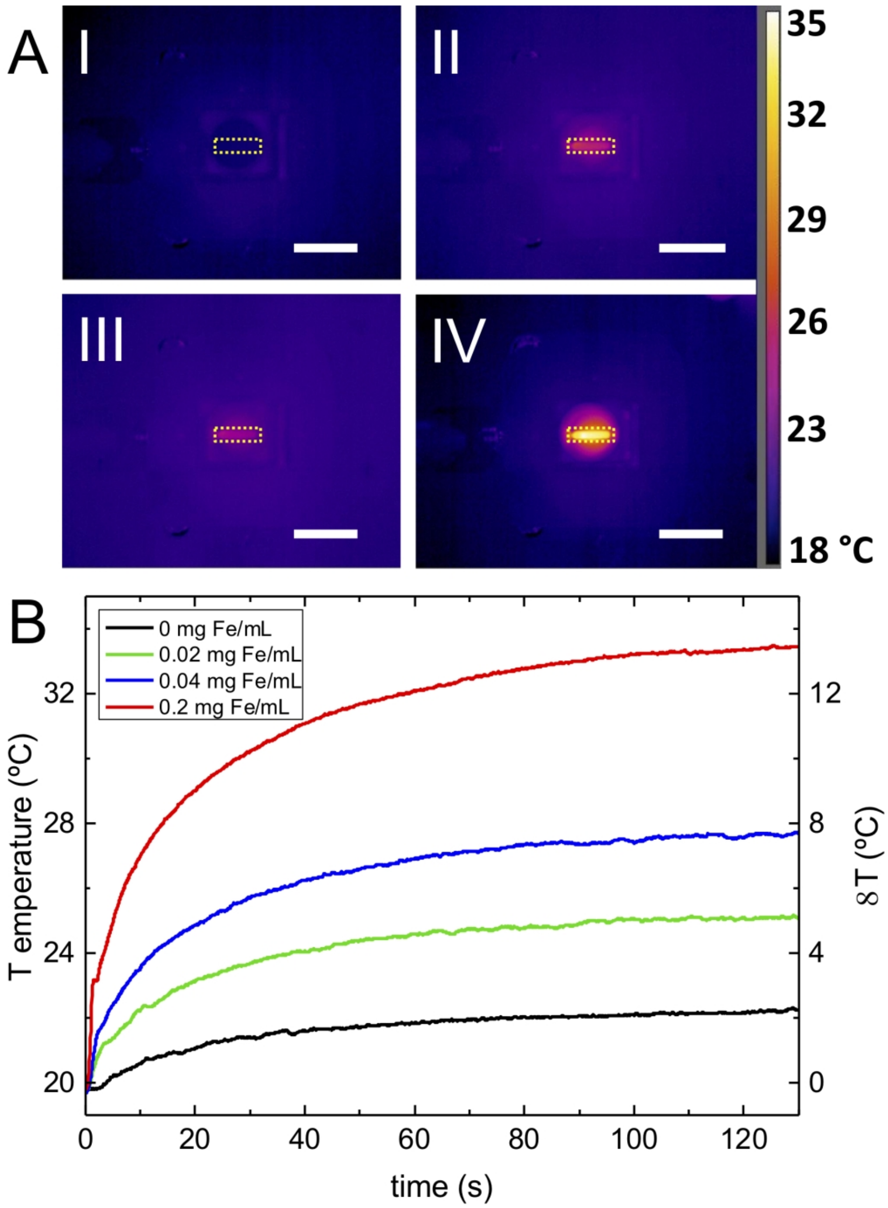

Figure 3. Photothermal effect of Fe-FexOy core-shell NWs. (A) Thermal images of the NW solutions in quartz micro-cuvettes acquired with an IR camera. (AI) PBS solution before laser irradiation. (AII) to (AIV) samples with 0, 0.02 and 0.20 mg Fe/mL, respectively, after 2 min of NIR laser irradiation at 808 nm. The laser was applied with 0.8 W/cm2, and the images show top views of the samples. The yellow rectangles indicate the area from which the average temperature was calculated. Scale bar = 1 cm. (B) Temperature response of the NW suspensions, when irradiated with a NIR laser (808 nm) at the concentrations of 0, 0.02, 0.04, and 0.20 mg Fe/mL.

167x222mm (300 x 300 DPI)

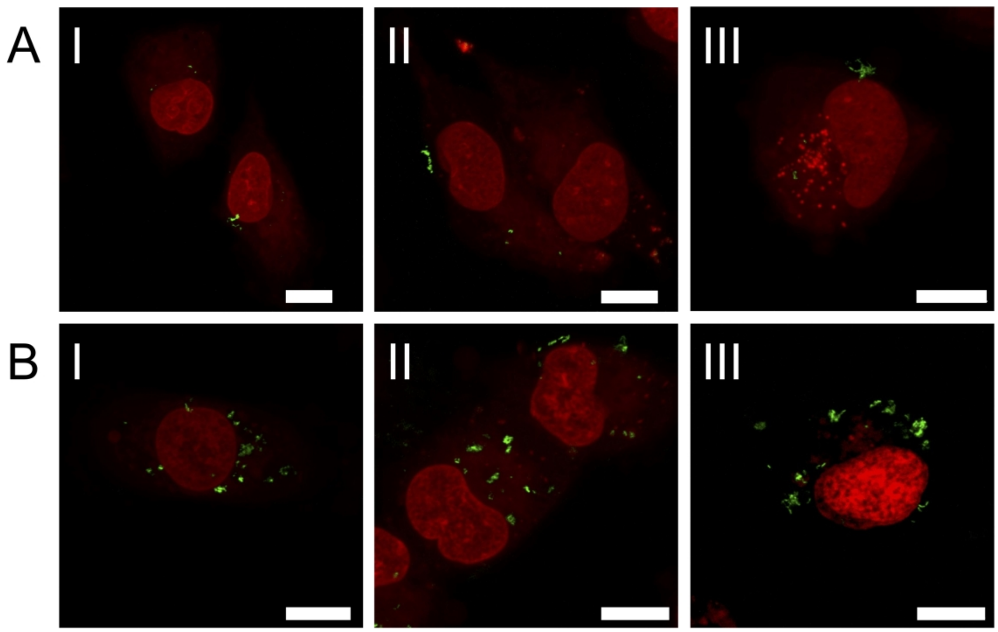

Figure 4. Confocal microscopy images of MDA-MB-231 cells incubated with BSA coated NWs. Cell incubated with BSA coated NWs after 24 h with a concentration of 0.01 mg Fe/mL (AI-AIII) and 0.02 mg Fe/mL (BI-BIII). Scale bars = 10 µm. NWs through light-reflected signal are shown in green and were pseudo-colored using ZEN-ZEISS imaging software. The nucleus, shown in red, was stained with NucRed™ Live 647. These are representative images of 3 independent experiments for each NW concentration.

225x140mm (300 x 300 DPI)

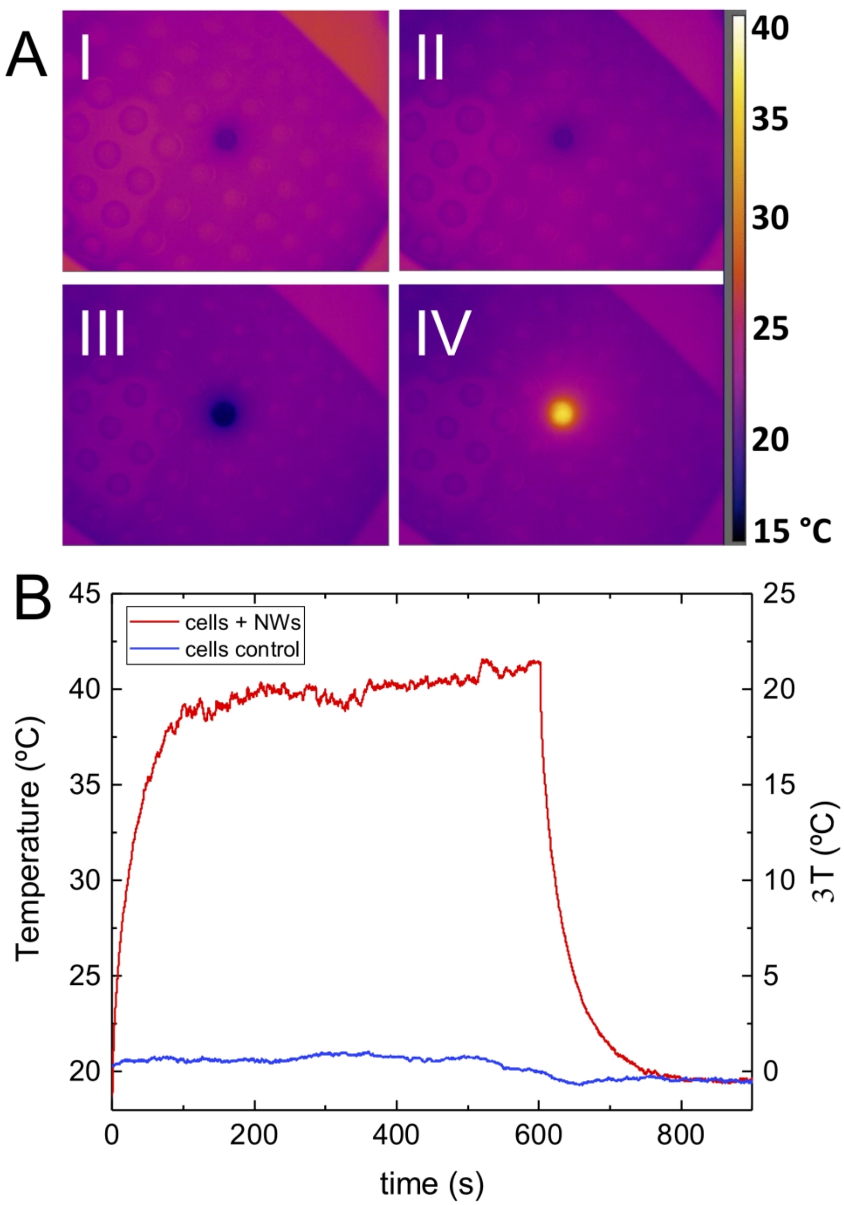

Figure 5. Photothermal effect of BSA coated NWs in breast cancer cells. (A) Thermal images acquired with an infrared camera of a concentrated suspension of breast cancer cells. Cells without NWs before (AI) and after (AII) NIR laser irradiation. Cells incubated with BSA coated NWs before (AIII), and after (AIV) NIR laser irradiation. The laser was applied with a power density of 0.8 W/cm2, and the images correspond to the view from the top of a 96 well plate. (B) Temperature response curves of concentrated suspensions of breast cancer cells non-incubated (control) and incubated with BSA coated NWs (0.02 mg Fe/mL) that were irradiated with a NIR laser (808 nm).

155x215mm (300 x 300 DPI)

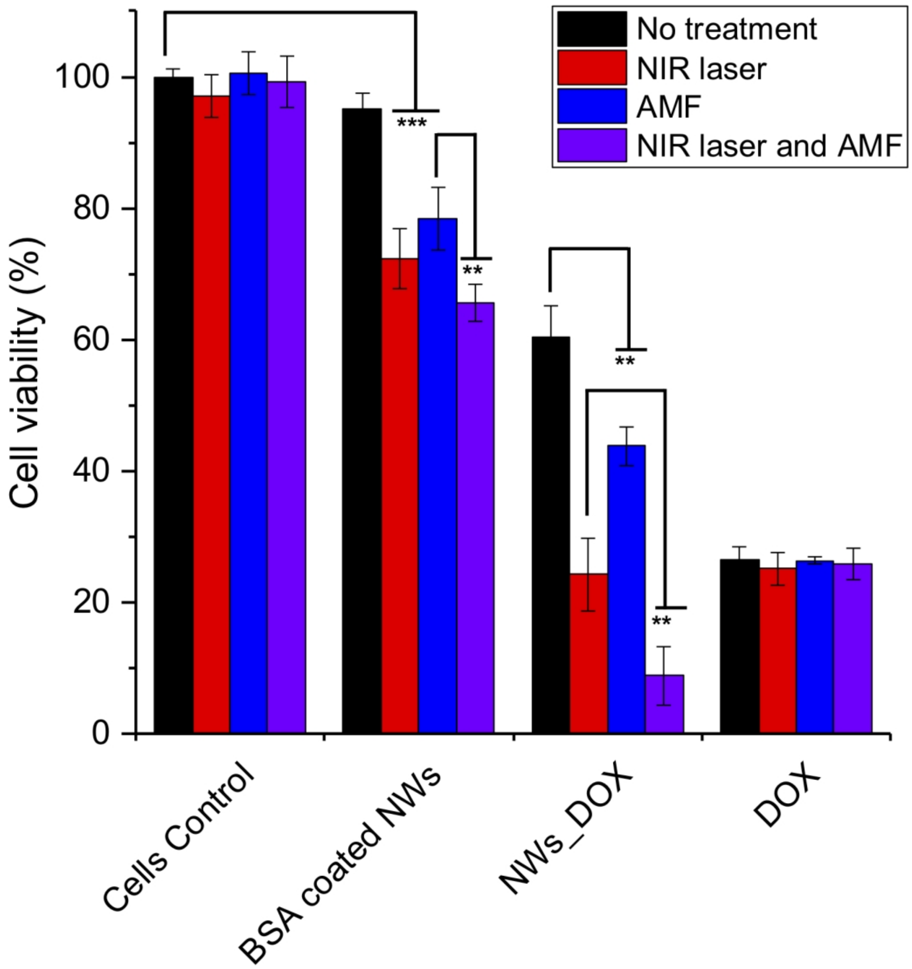

Figure 6. Viability of MDA-MB-231 cells incubated with different formulations of Fe-FexOy core-shell NWs with or without application of a low power AMF and/or NIR laser irradiation. BSA coated NWs: 0.02 mg Fe/mL, NWs_DOX: 0.02 mg Fe/mL and 1 μM of DOX. Free DOX: 1 μM. (*p < 0.05, **p < 0.01, and ***p < 0.001; n = 4).

161x158mm (300 x 300 DPI)